# Inter-technique validation of tropospheric slant total delays

**Michal Kačmařík[1], Jan Douša[2], Galina Dick[3], Florian Zus[3], Hugues Brenot[4], Gregor Möller[5], Eric Pottiaux[6], Jan Kapłon[7], Paweł Hordyniec[7], Pavel Václavovic[2], Laurent Morel[8]**

[1] Institute of Geoinformatics, Technical University of Ostrava, Ostrava, Czech Republic
[2] Geodetic Observatory Pecný, Research Institute of Geodesy, Topography and Cartography, Zdiby, Czech Republic
[3] Helmholtz Centre Potsdam - GFZ German Research Centre for Geosciences, Potsdam, Germany
[4] Royal Belgian Institute for Space Aeronomy, Brussels, Belgium
[5] Department of Geodesy and Geoinformation, Vienna University of Technology, Vienna, Austria
[6] Royal Observatory of Belgium, Brussels, Belgium
[7] Institute of Geodesy and Geoinformatics, Wroclaw University of Environmental and Life Sciences, Wroclaw, Poland
[8] GeF Laboratory, ESGT – CNAM, Le Mans, France

*Correspondence to*: M. Kačmařík (michal.kacmarik@vsb.cz)

**Abstract.** An extensive validation of line-of-sight tropospheric Slant Total Delays (STD) from Global Navigation Satellite Systems (GNSS), ray-tracing in Numerical Weather Prediction Models (NWM) fields and microwave Water Vapour Radiometer (WVR) is presented. Ten GNSS reference stations, including collocated sites, and almost two months of data from 2013, including severe weather events, entered the comparison. Seven institutions delivered their STDs based on GNSS observations processed using five software and eleven strategies enabling to compare rather different solutions and to assess the impact of several aspects of the processing strategy. STDs from NWM ray-tracing came from three institutions using three different NWM models and ray-tracing software. Inter-techniques evaluations demonstrated a good mutual agreement of various GNSS STD solutions compared to NWM and WVR STDs. The mean bias among GNSS solutions not considering post-fit residuals in STDs was -0.6 mm for STDs scaled in the zenith direction and the mean standard deviation was 3.7 mm. Standard deviations of comparisons between GNSS and NWM ray-tracing solutions were typically 10 mm +/- 2 mm (scaled in the zenith direction), depending on the NWM model and the GNSS station. Comparing GNSS versus WVR STDs reached standard deviations of 12 mm +/- 2 mm also scaled in the zenith direction. Impacts of raw GNSS post-fit residuals and cleaned residuals on optimal reconstructing of GNSS STDs was particularly evaluated at inter-technique comparison and for GNSS at collocated sites. The use of raw post-fit residuals is not generally recommended as they might contain strong systematic effects as demonstrated in case of station LDB0. Simplified STDs reconstructed only from estimated GNSS tropospheric parameters, i.e. without applying post-fit residuals, performed the best in all the comparisons, however, it obviously missed part of tropospheric signals due to non-linear temporal and spatial variations in the troposphere. Although the post-fit residuals cleaned from visible systematic errors generally showed a slightly worse performance, they contained significant tropospheric signal on top of the simplified model. They are thus recommended for the reconstructing STDs, particularly during a high variability in the troposphere. Cleaned residuals showed also a stable performance during ordinary days while containing promising information about the troposphere at low elevation angles.

## 1 Introduction

Tropospheric Slant Total Delay (STD) represents the total delay that undergoes the GNSS radio-signal due to the neutral atmosphere along the path from a satellite to a ground receiver antenna. This total delay can be separated into the hydrostatic part, caused by the dry atmospheric constituents, and the wet part caused specifically by water vapour. By quantifying the total delay, and by separating the hydrostatic and wet parts, it is possible to retrieve the amount of water vapour in the atmosphere along the path followed by the GNSS signal.

During the processing of GNSS observations only the total delay in the zenith direction (Zenith Total Delay, ZTD) above the GNSS antenna can be estimated for each epoch or for a time interval. ZTDs from GNSS reference stations are operationally assimilated into Numerical Weather Models (NWM) for almost a decade (Benitt and Jupp, 2012; Mahfouf et al., 2015). In Europe, this activity is coordinated mainly in the framework of the EUMETNET EIG GNSS Water Vapour Programme (E-GVAP, 2005-2017, Phase I-III, http://egvap.dmi.dk). Many recent studies demonstrated a positive impact of the ZTD or Integrated Water Vapour (IWV) assimilation on precipitation weather forecasts, especially of the short-time ones (Vedel and Huang, 2004; Guerova et al., 2006; Shoji et al., 2009; Guerova et al., 2016). On the other hand, continuous developments in NWM forecasting and nowcasting tools, as well as increasing needs for better predictions of severe weather events, stress the demand of high-quality humidity observations with high spatial and high temporal resolutions. While ZTDs provide information in zenith directions above GNSS stations, linear horizontal tropospheric gradients give information about the first-order spatial asymmetry around the station. Besides, Slant Tropospheric Delays (STDs) can provide additional details about the horizontal asymmetry in the troposphere, more specifically in the directions from a receiver to all observed GNSS satellites. With the increasing number of GNSS systems and satellites, the atmosphere scanning will be more complete, hence gaining even more interest. Bauer et al. (2011) showed a positive impact of STD assimilation into the Mesoscale Model 5 (MM5) and Kawabata et al. (2013) demonstrated a significant advantage of assimilating STDs into a high-resolution model in case of forecasting local heavy rainfall event against the scenario of assimilating ZTDs only. Also, Shoji et al. (2014) and Brenot et al. (2013) showed promising techniques for prediction of severe weather events using advanced GNSS tropospheric products such as horizontal gradients and STDs. The GNSS tomography technique aiming at the three-dimensional reconstruction of the water vapour field (Flores et al., 2001) uses STDs as input data as well. Obviously, the quality of the tomography depends on both the accuracy of the STDs (Bender et al., 2009) and the observation geometry (Bender et al., 2011).

Validation of GNSS slant delays with independent measurements is not a new research topic. GNSS slant delays were validated against WVR measurements in Braun et al. (2001), Braun et al. (2002) and Gradinarsky (2002). First attempts to derive slant delays from NWM fields and to compare them with GNSS STDs were carried out by De Haan et al. (2002) and Ha et al. (2002). Additional effort in evaluation of GNSS slant delays using WVR and NWM data was done at GFZ Potsdam during last years. Bender et al. (2008) showed an existing high correlation within the three sources (GPS, WVR, NWM) of slant wet delays and tried to quantify the effect of removing multipath from GPS post-fit residuals using a stacking method what was also done by Kačmařík et. al (2012). Deng et al. (2011) validated tropospheric slant path delays derived from single- and dual-

frequency GPS receivers with NWM and WVR data. Shang-Guan et al. (2015) compared GPS versus WVR slant IWV values (SIWV) using a 184-day long dataset. They also analysed the influence of the elevation angle setting and the meteorological parameters (used for the conversion to IWV) on the comparison results. More recently, a validation of multi-GNSS slant total delays retrieved in real-time from GPS, GLONASS, Galileo and BeiDou constellation was presented by Li et al. (2015a) using WVR and NWM as independent techniques for the assessment. Using multiple GNSS constellations brought a visible advantage, not only in terms of number of available slants, but also in their higher accuracy and robustness.

Nevertheless, most of the so-far presented studies were limited to only a single strategy for obtaining GNSS STDs, and usually restricted to a limited set of stations and/or a relatively short time period. The main purpose of this study is an extensive comparison of various solutions from GNSS processing, NWM ray-tracing and WVR measurements using one common dataset, and also comparing results from collocated stations. The GNSS solutions evaluated in this work used five different software and eleven strategies, and exploited the GNSS4SWEC benchmark dataset (Douša et al., 2016). Then, the paper studies the impact of various approaches on STD estimates and aims at finding the most suitable strategy for estimating the GNSS-based STDs.

Section 2 briefly introduces the validation study dataset, and Section 3 describes the process of retrieving GNSS STDs including an overview of the different GNSS solutions. Section 4 provides a description of STDs generated from NWMs, and Section 5 summarizes WVR principals and WVR-based STD solutions. Section 6 introduces the methodology used in the validation of STDs, and Sections 7 and 8 study the results achieved at single GNSS reference stations and at closely collocated stations, respectively.

## 2 Experiment description

The presented work has been carried out in the context of the EU COST Action ES1206 "Advanced Global Navigation Satellite Systems tropospheric products for monitoring severe weather events and climate (GNSS4SWEC)" (http://www.cost.eu/COST_Actions/essem/ES1206, 2013-2017). Three mutually cooperating Working Groups (WG) have been established to cover the proposed topics: 1) WG1: Advanced GNSS processing techniques, 2) WG2: GNSS for severe weather monitoring, and 3) WG2: GNSS for climate monitoring. Validation of STDs belongs mainly under WG1, which is besides other topics oriented toward the development of new advanced tropospheric products. The idea of preparing a common benchmark dataset, which could serve efficiently for most planned activities, was designed in the beginning of the project, and the data were collected, cleaned, documented, reference products generated and assessed (Douša et al., 2016). The selected geographical area is situated in central Europe (Austria, Germany, the Czech Republic, Poland) where severe weather events, including extensive floods on Danube, Moldau and Elbe rivers, occurred between May and June 2013. The benchmark dataset gathers observations from 430 GNSS reference stations, 610 meteorological synoptic stations, 21 radiosonde launching sites, 2 Water Vapour Radiometers (WVR), 2 meteorological radars, and output fields from the ALADIN-CZ Numerical Weather Prediction (NWP) model over a period of 56 days. ZTDs and horizontal tropospheric gradients from the reference GNSS and

NWM-derived tropospheric products were already evaluated, and all resulted in very good agreements (Douša et al., 2016). All STDs used in this paper were computed by exploiting the benchmark dataset.

From the complete benchmark dataset, we selected a subset of 10 GNSS reference stations situated at six different locations (Table 1). The selection was based on the following requirements: 1) long-term quality of observations and its stability, 2) availability of another GNSS reference station in the site vicinity, 3) availability of another instrument capable of STD measurements in the site vicinity, and 4) the location of the station w.r.t. its altitude and the weather events which occurred during the evaluation period. The subset also includes collocated (dual) GNSS stations playing an important role in the validation. The collocated stations observed GNSS satellites with the same azimuth and elevation angles, so that they should theoretically deliver the same or very similar tropospheric parameters – ZTD, linear horizontal gradients and slant delays. Post-fit residuals of carrier-phase observations at the collocated stations should represent common effects due to the local tropospheric anisotropy, while systematic differences could remain due to instrumentation and environmental effects such as antenna and receiver characteristics, and multipath. Only STDs from the WVR at Potsdam, collocated with the GNSS stations POTM and POTS, were available for this study because the second WVR, located at Lindenberg and collocated with the GNSS stations LDB0 and LDB2, was operated only in the zenith direction during the period of the study.

## 3 Slant Total Delay retrievals from GNSS observations

The tropospheric Slant Total Delay (STD) cannot be estimated directly from GNSS data since the total number of unknown parameters in the solution would be higher than the number of observations. Instead, the total delays in the zenith direction above the GNSS station (i.e. ZTD) are adjusted together with, optionally, total tropospheric linear horizontal gradients (*G*) to account for the first-order asymmetry of the local troposphere. The estimates are valid for individual processing epochs whenever using a stochastic approach, or for a given time interval when modelling the troposphere with a deterministic process, e.g. by a piece-wise constant or linear model.

In practice, the ZTD is decomposed into an a priori model, usually by introducing the Zenith Hydrostatic Delay (ZHD, see Saastamoinen, 1972), and the estimated corrections, representing (mainly) the Zenith Wet Delay (ZWD). Similarly, the STD is decomposed to the *ZHD*, *ZWD*, *G* and post-fit residuals (*RES*) as described in Eq. (1), where *ele* is the elevation angle and *azi* is the azimuth angle in degrees. The STD value is given in meters.

$$STD(ele, azi) = ZHD \cdot mf_h(ele) + ZWD \cdot mf_w(ele) + G(ele, azi) + RES \quad (1)$$

The elevation angle dependency of STD is described by the mapping functions, separately for the hydrostatic ($mf_h$) and the wet ($mf_w$) components. Nowadays, the Vienna Mapping Function (VMF1, see Böhm et al., 2006a) - or VMF1 like concept - is commonly used in GNSS data processing. Also, the empirical mapping function 'Global Mapping Function' (GMF, see

Böhm et al., 2006b) is popular since it is consistent with VMF1 and easier to implement (independent on external data needing updates). Both, the VMF1 and the GMF are applicable down to 3° elevation angles.

The first-order horizontally asymmetric delay *G(ele,azi)* in Eq. (1) reflects local changes in temperature and particularly in water vapour. MacMillan (1995) proposed a model describing the gradient delay as a function of the elevation and azimuth angles:

$$G(ele, azi) = mf_g \cdot (G_N \cdot cos(azi) + G_E \cdot sin(azi)) \quad (2)$$

where $mf_g(ele) = mf_h(ele) \cdot cot(ele)$. Chen and Herring (1997) replaced the elevation dependent term $mf_h(ele) \cdot cot(ele)$ by the gradient mapping function $mf_g(ele) = 1/(sin(ele) \cdot tan(ele) + C)$, with $C = 0.0032$, nowadays commonly used in GNSS data processing. Typical range for $G_N$ and $G_E$ is below 1-2 mm, however, gradients can reach up to 7 mm during extreme weather events. The gradient of 1 mm corresponds to about 55 mm slant delay correction when projected to 7° elevation angle.

Additionally, post-fit residuals *RES* may contain un-modelled tropospheric effects not covered by the estimated tropospheric parameters. Such remaining effects are supposed to be caused mainly by higher spatial and temporal variations of the humidity or its significant horizontal asymmetry in the troposphere. Obviously, residuals contain also other un-modelled effects such as multipath, errors in antenna phase centre variations or satellite clocks. For eliminating such systematic effects, cleaning of post-fit residuals is applied by generating elevation/azimuth-dependent correction maps as described by Shoji et al. (2004). For each solution and each station, we thus computed mean values of post-fit residuals in 1×1 degree bins using the whole benchmark period. Residuals exceeding ±3 times the standard deviation were excluded from the computation of the mean. Computed means were then subtracted from the original post-fit residuals to generate solutions using cleaned residuals.

For the analysis of GNSS L1 and L2 carrier-phase observations, the least-squares adjustment or Kalman-filter approach was applied to estimate the ZWDs and the two horizontal gradient components $G_N$ and $G_E$ at each GNSS site (Table 1). Afterwards, Eq. (1) was used to compute STDs for each satellite in view. Whenever zero-differenced (ZD) post-fit residuals were available for any solution, three variants of the solution are presented in the paper: 1) solution without residuals (nonRES), 2) solution with raw residuals (rawRES), and 3) solution with cleaned residuals (clnRES).Seven institutions delivered their STD solutions for this validation study, namely Ecole Supérieure des Géomètres et Topographes (ESGT CNAM), Geodetic Observatory Pecný (GOP, RIGTC), Helmholtz Centre Potsdam - German Research Centre for Geosciences (GFZ), Royal Observatory of Belgium (ROB), Technical University of Ostrava (TUO), Vienna University of Technology (TUW), and Wroclaw University of Environmental and Life Sciences (WUELS). Principal information about individual solutions are given in Table 2 with a few specific notes important for the interpretation of the results.

GOP delivered two solutions based on the Precise Point Positioning (PPP) technique (Zumberge et al., 1997) and using the in-house developed application Tefnut (Douša and Václavovic, 2014) derived from the G-Nut core library (Václavovic et. al., 2013). Considering all available GNSS solutions, only GOP used a stochastic modelling approach to estimate all parameters.

Additionally, GOP provided two solutions: 1) GOP_F using Kalman filter (forward filter only), i.e. capable of providing ZTD, tropospheric gradients and STDs in real time, and 2) GOP_S applying the backward smoothing algorithm (Václavovic and Douša, 2015) on top of the Kalman filter in order to improve the quality of all estimated parameters during the batch processing interval and for avoiding effects such as the PPP convergence or re-convergence.

Some institutions delivered also two STD solutions which differ in a single processing setting. The aim was to evaluate their impact on STDs: a) TUO_G and TUO_R exploit GPS-only and GPS+GLONASS observations respectively, b) TUW_3 and TUW_7 apply an elevation cut-off angle of 3 and 7 degrees respectively, and c) ROB_G and ROB_V use the GMF and VMF1 mapping functions respectively. Additionally, ROB solutions are the only ones based on the processing of double-difference (DD) observations and providing ZD carrier-phase post-fit residuals converted from the original DD residuals using the technique described in Alber et al. (2000). For other DD solutions, variants without adding residuals were compared only.

In total, we validated eleven solutions computed with five different GNSS processing software. Five of the solutions used GPS and GLONASS observations and six solutions used GPS-only observations; five of them are based on double-difference observations and six of them are computed using zero-difference data in PPP analysis. More information about TUW solutions can be found in Möller et al. (2016), about GFZ in Bender et al. (2009, 2011), Deng et al. (2011) and about CNAM in Morel et al. (2014). For ROB, TUO and WUE solutions we refer the reader to Dach et al. (2015).

## 4 Computation of Slant Total Delay from Numerical Weather Prediction model

Simulating STDs in NWP models consists in integrating the atmospheric refractivity through the path followed by GNSS signals. STDs have been simulated using three different NWMs: ALADIN-CZ (4.7 km-resolution limited-area hydrostatic model, operational analysis in 6h interval with forecasts for 0, 1, 2, 3, 5, 6 h, http://www.umr-cnrm.fr/aladin/), ERA-Interim (1° horizontal resolution, 6h reanalysis), and NCEP-GFS (1° horizontal resolution, 6h operational analysis, https://www.ncdc.noaa.gov/data-access/model-data/model-datasets/global-forcast-system-gfs). None of these NWM assimilates data from ground GNSS stations. For more information about the models, see Douša et al. (2016) and specifically Trojáková (2016) for ALADIN-CZ model and Dee et al. (2011) for ERA-Interim. First, STD solutions using the ERA-Interim and NCEP-GFS models were delivered by GFZ Potsdam using acronym ERA/GFZ and GFS/GFZ, respectively. Only a short introduction is provided in Section 4.1 since the GFZ tool for ray-tracing has been described in other papers cited below. Two STD solutions were then delivered for the ALADIN-CZ model: a) the ALA/BIRA, which was generated at Royal Belgian Institute for Space Aeronomy (BIRA), described in Section 4.2, and b) the ALA/WUELS, which was delivered by Wroclaw University of Environmental and Life Sciences, described in Section 4.3.

### 4.1 Description of ERA-Interim STD solution (ERA/GFZ) and NCEP-GPS STD solution (GFS/GFZ)

The ERA-Interim and NCEP-GFS STD solutions by GFZ are based on 'assembled' STDs. At first, for the considered station and epoch, a set of ray-traced STDs (various elevation and azimuth angles) is computed using technique described in Zus et

al. (2014). Secondly, from this set of ray-traced STDs, the tropospheric parameters (i.e. zenith delays, mapping function coefficients, first- and higher-order gradient components) are determined. Finally, for the required azimuth and elevation angle the STD is 'assembled' using the tropospheric parameters. For a detailed description of the tropospheric parameter determination the reader is referred to Douša et al. (2016). The differences between the 'assembled' and ray-traced STDs are sufficiently small in particular for elevation angles above 10° (Zus et al., 2016). In essence, the largest uncertainty in the 'assembled' (and ray-traced) STDs remains the uncertainty of the underlying NWM refractivity field. This uncertainty is estimated to be about 8-10 mm close to the zenith increasing to about 8-10 cm at an elevation angle of 5 ° (Zus et al., 2012). Similar uncertainty of around 8 mm for the zenith direction was also found for ALADIN-CZ model in Douša et al. (2016).

### 4.2 Description of ALADIN-CZ STD solution from BIRA (ALA/BIRA)

To compute STDs from ALADIN-CZ, a simplified strategy has been used to model the curve path followed by GNSS signals through the neutral atmosphere, as suggested by Saastamoinen (1972). The delays simulated with this strategy show small differences in comparison to straight line simulations (differences of about 4 mm, 5 mm and 10 mm respectively at 15°-, 10°- and 5°-elevation). Simulations have computed STDs down to 3°-elevation, however, under an elevation of 15°, a proper ray tracing strategy, as mentioned in Section 4.1, should be preferably applied.

For each latitude-longitude grid point and each level of ALADIN-CZ model, the NWP outputs considered to compute STDs are: geopotential height (*geopotH* in m), pressure (*P* in Pa), temperature (*T* in K), partial pressure of water vapour (*e* in Pa), mixing ratio of liquid and solid water (in kg/kg). The ground pressure of each column is also retrieved. The geopotential height is converted to the altitude above the geoid:

$$h_{geoid} = (g_0 * R_e * geopotH) / (g * R_e - g_0 * geopotH) \quad (3)$$

where $g_0$ is a standard gravity acceleration (mean value of $9.80665\ m/s^2$ from the World Meteorological Organization, WMO); $R_e = 6378137 / (1.006803 - 0.006706 * \sin^2(lat))$ is the radius of the ellipsoid in meter for the latitude (*lat* in degrees); *g* is the gravity acceleration (in m/s²) of the considered location given as:

$$g = 9.7803267714 * (1. + 0.00193185138639 * \sin^2(lat)) / \sqrt{1. - 0.00669437999013 * \sin^2(lat)} \quad (4)$$

Then, the height above the geoid is converted to height above the WGS84 ellipsoid (in m) with the use of the EGM96 (Earth Gravitational Model, Lemoine et al., 1998) undulation. Note that for the region of the benchmark campaign the difference between geoid and WGS84 altitude is about 47 m.

Using the hypsometric equation, the ground pressure and the pressure of each level are considered to estimate the altitude for the different levels. In total ALADIN-CZ outputs provide 87 levels up to an altitude of about 55 km. However, to assess STDs from ALADIN-CZ, the integration was stopped at 15 km since the contribution of water vapour above this altitude is negligible. An adaptive step is considered (100 m, 200 m, 250 m, 500 m, 1000 m, respectively for vertical altitudes between 0-1 km, 1-3

km, 3-5 km, 5-10 km, 10-15 km). Bi-linear interpolations of ALADIN-CZ parameters at the altitude of the GNSS station and for each step of the integration were proceeded. Note that there is no station selected for the validation located below the first layer of ALADIN-CZ.

The expression of simulated STDs from ALADIN-CZ is the summation of these four contributions:

$$STD = SHD_{int} + SWD_{int} + SHMD_{int} + STD_{ext} \quad (5)$$

where $SHD_{int}$, $SWD_{int}$ and $SHMD_{int}$ are respectively the inside-model integration contribution of the hydrostatic, wet and hydrometeor delays, and $STD_{ext}$ is the external model contribution (over 15 km).

$$SHD_{int} = 10^{-6} \sum_{k=1}^{k=k_{top}} k_1 \frac{P_i}{Tv_i} \Delta s_i \quad (6)$$

$$SWD_{int} = 10^{-6} \sum_{k=1}^{k=k_{top}} \left( k'_2 \frac{e_i}{T_i} + k_3 \frac{e_i}{T_i^2} \right) \Delta s_i \quad (7)$$

with $k'_2 = k_2 - k_1 * R_d / R_w$ where $k_1$ (in K/Pa), $k_2$ (in K/Pa), $k_3$ (in $K^2$/Pa) are the empirical refractivity coefficients of Bevis et al. (1994), $R_d$ and $R_w$ the gas constants respectively for dry air and water vapour (in J/kmol K), and $T_v$ is the virtual temperature (in K). For the estimation of the hydrometeor contribution inside the model, as presented in Eq. (8), ($N_{lw}$, $M_{lw}$) and ($N_{ice}$, $M_{ice}$) are (atmospheric refractivity, mass content per unit of air volume) of the liquid and ice water, respectively.

$$SHMD_{int} = 10^{-6} \sum_{k=1}^{k=k_{top}} (N_{lw} + N_{ice}) \Delta s_i = \sum_{k=1}^{k=k_{top}} (\alpha_{lw} M_{lw} + \alpha_{ice} M_{ice}) \Delta s_i \quad (8)$$

The estimation of coefficients $\alpha_{lw} \sim 1.45$ and $\alpha_{ice} \sim 0.69$ is presented in Brenot et al. (2006). The ALADIN-CZ model provides mixing ratios of cloud water (liquid components) and pristine ice (solid water components). The mass content per unit of air volume is obtained using the associated mixing ratio, pressure, water vapour partial pressure and temperature.

$STD_{ext}$ is obtained with the hydrostatic formulation (Saastamoinen, 1972) mapped with $mf_h$ (see Eq. 1) and using the elevation, latitude and pressure of the last step of the integration (i.e. at 15 km). Note that the wet contribution over 15 km is neglected since it is practically zero. The estimation of $STD_{ext}$ (about 0.21 m) provides sufficiently accurate modelling for the hydrostatic contribution over 15 km (as shown by the sensitivity test from Brenot et al., 2006).

### 4.3 Description of ALADIN-CZ solution from WUELS (ALA/WUELS)

The ray-traced tropospheric delays for WUELS solution are based on piece-wise bent-2d model propagation. Thus, it prevents to know the exact trajectory in advance in contrary to straight-line model and needs to be solved iteratively based on preceding

ray refractive index. Similar examples are given by Böhm and Schuh (2003) or Hobiger et al. (2008). We assume the ray-path does not leave the plane of constant azimuth for a given elevation angle to a satellite. The out-of-plane contribution to the delay is thus neglected making the propagation two-dimensional, hence 2d. The real ray-path is then approximated by a finite number of linear ray-pieces in WGS84 coordinates using Euler formula for Earth radius

$$R = (\cos^2 A / M + \sin^2 A / N)^{-1} \quad (9)$$

where $A$ is the azimuth angle between a satellite and a receiver, $M$ and $N$ are radii of curvature along meridian and prime vertical, respectively. We follow height-dependent increments as presented in Rocken et al. (2001): 10 m, 20 m, 50 m, 100 m, 500 m respectively for geometric altitudes between 0-2 km, 2-6 km, 6-16 km, 16-36 km, and above 36 km which require meteorological parameters to be vertically interpolated in order to obtain finer resolution. Both $P$ and $e$ are interpolated exponentially from two nearest layers, while the temperature change is considered linear. Horizontally, we find the four nearest nodes for each ray to perform weighted mean interpolation, where the weighting function equals to the inverse squared distance. The reference hybrid-level of the ALADIN-CZ model is determined by surface geopotential which is converted to geopotential meters by dividing the geopotential values by $g_0$. Meteorological parameters are expressed on pressure levels which represent standard vertical coordinate. The hypsometric equation is used to calculate geometric thickness between consecutive isobaric surfaces

$$dz = R_d * T_m / g_0 * \ln(P_1 / P_2) \quad (10)$$

where $R_d = 287.058\ JK^{-1}kg^{-1}$ is the gas constant for dry air, $T_m$ is the mean virtual temperature of the layer between $P_1$ and $P_2$ pressure levels in Kelvin. The conversion from ALADIN-CZ vertical coordinate system to geometric altitudes is then consistent with the BIRA approach described in Section 4.2. In WUELS solution, the signal tracking is performed exploiting a full model vertical resolution up to the uppermost ALADIN-CZ layer at 55 km. Above the top layer, we adopt the U.S. Standard Atmosphere (1976) to provide supplementary meteorological data up to 86 km. For each ray-path coordinates, the refractive index is calculated as a function of *P (in hPa)*, *e (in hPa)* and *T (in K)* with empirically derived "best available" coefficients $k$ given by Rueger (2002).

$$N = (n - 1) \times 10^6 = k_1 * (P - e)/T + k_2 * e/T + k_3 * e/T^2 \quad (11)$$

The contribution of water droplets and ice crystals in the atmosphere is neglected in the total delay. All tropospheric delays are traced with respect to vacuum elevation angles. The electromagnetic delay is calculated for a given chord length ($s$) using the mean refractive index $n$ between two consecutive rays yielding the total delay in meters

$$STD = \sum s_i(n_i - 1) \times 10^6 \quad (12)$$

which can be separated on hydrostatic and wet part using respective refractive indices. Additionally, to the radio path length, the accumulated bending effect (*bend*) along the ray path is added to the hydrostatic mapping function which, together with the wet mapping function, can be calculated as follows:

$$bend = \sum (s_i - cos(ele_i - ele_k)\, s_i) \quad (13)$$

$$mf_h = (SHD + bend) / ZHD \quad (14)$$

$$mf_w = SWD/ZWD \quad (15)$$

where $ele_i$ is the elevation angle for a given model layer and $ele_k$ is the outgoing elevation angle at uppermost altitude.

### 4.4 Assessment of the Hydrostatic, Wet and Hydrometeor Contributions to the Slant delays

ALADIN-CZ NWM has been used to estimate the Hydrostatic, Wet and Hydrometeor contributions to slant delays. During the whole period of the benchmark campaign, the maximum contribution of hydrometeors reached 17 mm at the zenith during the extreme weather events on 20-23 June (Douša et al., 2016). The 2D fields of ZTD, ZHD, ZWD, and ZHMD (zenith hydrometeor delays) are presented in Figure 1. They illustrate the large-scale convection with the presence of hydrometeors along the convergence line associated with a strong contrast of dry and wet air masses. The contribution of hydrometeors to ZTD reached up to 7 mm (as scaled in the zenith direction) for the stations POTS and POTM at 15:00 UTC on 23 June 2013 (see Figure 1d). According to satellite trajectories at this time for the station POTS, a maximum SHMD of 25.6 mm is observed for a satellite at 22°-elevation angle.

Figure 2 shows simulated differential STDs for a cone with a 10° elevation angle during the severe weather condition of the 23rd of June 2013, and mapped in the zenith direction (at 90°) using the mapping functions of Eq. (1): $mf_h$ for SHD and $mf_w$ for SWD and SHMD. For this 10°-cone, the minimum present values of total, hydrostatic, wet and hydrometeors delays simulated at 15:00 UTC on 23 June, are given as STDmin, SHDmin, SWDmin and SHMDmin in Figure 2. The respective differences of STD, SHD, SWD and SHMD and corresponding minimum values simulated at 15:00 UTC are presented in Figure 2. The anisotropic variation of total, hydrostatic, wet and hydrometeor delays can be visualised on a skyplot. As a confirmation of Figure 1b and 1d, Figure 2 shows weak hydrostatic anisotropy. This anisotropy (up to 5.8 mm) is almost the same as the hydrometeors one (up to 6 mm). The area within the red curve is larger than the purple area (hydrostatic anisotropy), meaning that the total effect of the hydrometeor anisotropy is slightly larger than the one from the hydrostatic component. Note that Figure 2 shows the anisotropies simulated at 10° and mapped at 90° (giving an idea of the variations in the zenith direction). The largest anisotropy is clearly induced by water vapour (values up to 20 mm in the south-east direction of POTS, also shown in Figure 1c). With mean hydrostatic and hydrometeor anisotropies oriented in the opposite direction of the wet one, Figure 2 presents a total anisotropy with weaker values (up to 12 mm) than the wet anisotropy.

To complement the snapshot of Figure 2 the time-evolutions of SHD, SWD, SHMD, and STD in the direction of all observed GNSS satellites for the station POTS are presented in Figure 3. Slant delays have been simulated in the direction of observed satellites (hydrostatic, wet, hydrometeor and total contributions) and, to avoid the effect of the elevation and to look at the same order of magnitude of delays, corresponding delays in the zenith direction have been computed and mapped using mapping functions presented in Eq. 1 ($mf_h$ for SHD and $mf_w$ for SWD and SHMD). These values ($STD_{min}$ = 2310.6 mm, $SHD_{min}$ = 2240.8 mm, $SWD_{min}$ = 43.1 mm and $SHMD_{min}$ = 0 mm) obtained during the whole period of the benchmark campaign, have been subtracted from their corresponding values simulated in direction of satellites. Then, the differences have been mapped back at 90°. For day of year (DOY) 174 (i.e. 23rd of June 2013), we can see a contribution of hydrometeors up to 10 mm. Looking at the whole period of the benchmark campaign, the variation range of STD, SHD and SWD (mapped at 90°) are 275 mm, 80 mm and 230 mm, respectively. Figure 3 illustrates the interest of GNSS delay observations for meteorology (detection of variation of water vapour represented by the wet delay, but also detection of heterogeneities from hydrostatic delays and occasionally from hydrometeors in specific severe weather cases). Note that there is no data available for POTS station between DOY 121 and 125 and DOY 160 and 163. For this reason, we have not simulated the slant delays for this period, as shown by the gaps in Figure 3. The simplified strategy used to simulate curve slant paths gives some inaccurate simulations of slant delays for elevations between 3° and 5°, shown by isolated values in Figure 3. Such inaccuracies could be avoided by using a ray-tracing algorithm. For a comprehensive overview on ray-tracing algorithms and comparisons the reader is referred to Nafisi et al. (2012).

## 5 Water Vapour Radiometer Measurements

During the benchmark period, the WVR located at GFZ Potsdam operated in a mode scanning the atmosphere at selected elevation and azimuth angles. The instrument is situated on the same roof as the GNSS reference stations POTM and POTS. All three devices are within ten meters from each other. The HATPRO WVR from Radiometer Physics was set up to scan the atmosphere to extract profiles of atmospheric temperature, water vapour and liquid water using frequencies between 22.24 and 27.84 GHz and a window channel at 31.4 GHz. The WVR is switching between 'zenith mode' when it is measuring Integrated Water Vapour (IWV) and 'slant mode' when it is tracking GPS satellites using an in-built GPS receiver. In the latter case, Slant Integrated Water Vapour (SIWV) values are delivered for the direction of satellites. Since the instrument can track only one satellite at one moment the number of observations is quite limited compared to slants from GNSS which are simultaneously observed from several GNSS satellites.

Our study focuses on the comparison of STDs, not SIWV. It was thus necessary to convert the WVR SIWV into STDs. Firstly, WVR observations with rain flag and Atmospheric Liquid Water (ALW) values exceeding 1 $kg*m^{-2}$ were rejected. Both rain and high values of ALW can significantly distort the quality of WVR measurements. Secondly, SIWV values were converted into Slant Wet Delays (SWD) using the Askne and Nordius (1987) formula and the refractivity constants from Bevis et al. (1994). ZHD values were computed with the precise model given by Saastamoinen (1972). For the described conversions, we

used values of the atmospheric pressure and temperature measured in situ of the GNSS reference station POTS. A hydrostatic correction for the altitude difference between the meteorological station and the WVR position was applied to the atmospheric pressure values. ZHD values were mapped to elevation angles of the WVR using the hydrostatic mapping function derived from the NCEP-GFS (Douša et al., 2016). In order to convert accurately SIWV to STDs, we took into account the influence of the hydrostatic horizontal gradients (see e.g. Li et al., 2015b). We used the hydrostatic horizontal gradients derived from the NCEP-GFS for that purpose. Finally, SHD and SWD values were summed up to deliver STDs. The described conversion of WVR SIWVs to STDs aimed at minimum distorting the accuracy of original WVR observations.

## 6 Methodology of STD comparisons

We provide the specificities of each type of technique comparisons in this section. Since NWM outputs are restricted to the time resolution of their predictions (typically one, three or six hours) and since WVR is able to track only one satellite at one moment, all three sources provide different numbers of STDs per day. Therefore, three different comparisons are presented: 1) results for GNSS versus GNSS comparisons, 2) results for GNSS versus NWM comparisons, and 3) results for GNSS versus WVR comparisons. Section 7 presents the validation at individual stations and Section 8 inter-compare results obtained at GNSS dual stations. All the given results are obtained over the whole benchmark period. No outlier detection and removal procedure was applied during the statistics computation within the study.

Two variants of the comparisons are presented: 'ZENITH' and 'SLANT'. 'ZENITH' stands for original STDs mapped back to zenith direction using *1/sin(e)* formula. Such mapping aimed at normalizing STD differences for their evaluation in a single unit. The 'SLANT' type of comparison denotes an evaluation of STDs at their actual elevation angles. To be more specific, slant delays were grouped into individual elevation bins of 5 degrees, i.e. for example all slants with an elevation angle between 10 and 15 degrees were evaluated as a single unit. There was one exception regarding the size of a bin since the lowest one contained slants from 7° to 10° elevation angle, 7° being the lowest elevation angle common to all GNSS STD solutions. This cut-off angle was thus used in all GNSS versus GNSS and GNSS versus NWM comparisons.

Presented values of biases and standard deviations were computed directly from all STDs within the processed benchmark campaign period, therefore they are not based on any kind of daily or other averaging. In some tables, only median values of bias and standard deviation over all GNSS STD solutions (Tables 5, 7 and 8) or over all processed stations (Tables 3 and 4) are given to consolidate the presentation of validation results. Median was used as a parameter minimally affected by outliers.

### 6.1 GNSS versus GNSS comparisons

In the case of individual inter-GNSS solutions validation, the situation was straightforward and no interpolation nor specific hypothesis was necessary: the comparisons were done on a direct point-to-point basis of observations coming from identical azimuth and elevation directions.

### 6.2 GNSS versus WVR comparisons

To find pairs of STDs observations between WVR and GNSS, the following rules were used: 1) the time difference between both observations had to be shorter than 120 s, and 2) the difference between both azimuth and elevation angles had to be smaller than 2.5° and 0.25°, respectively. From these criteria, the maximum difference in elevation angle has the largest impact on the number of observation pairs found. Hence the smaller values for these settings, the smaller number of pairs found and the smaller standard deviations resulted between GNSS and WVR STDs. As an illustration, a change from 0.35° to 0.25° led to the decrease of the number of STD pairs between the GNSS GFZ solution and the WVR at station POTS from 63,703 to 48,583 pairs; the standard deviation of the projected STD differences in the zenith direction then decreased from 14.6 to 11.7 mm too. Since the bias practically remained unchanged (-6.1 mm versus -5.9 mm), the applied selection procedure mainly influenced the stability of the comparison between WVR and other sources of slant delays. When comparing GNSS versus WVR STDs, a cut-off elevation angle was set to 15 degrees to exclude low-elevation angle observations from WVR as their quality could be further degraded by a ground radiation or other local environment conditions.

### 6.3 GNSS versus NWM comparisons

Given the very small distances between collocated antennas and the coarse resolution of the global NWM models, STDs from NWM ray-tracing using the ERA-Interim and the NCEP GFS models were derived only for one of the collocated stations. The same set of NWM-derived STDs was then used for the validation of the results at the collocated receivers.

## 7 Results at individual stations

### 7.1 GNSS versus GNSS

The total STD pairs available for this part of the validation is roughly 1.7 million, and varies from 140,987 to 206,320 according to the station.

#### 7.1.1 Evaluation of all GNSS solutions versus the reference GNSS solution

Individual GNSS solutions were first compared to the GFZ solution in the zenith direction (ZENITH). We chose the ‘GFZ’ solution as the reference because GFZ Potsdam has long-term experience in producing GPS slant delays and because the GFZ near real-time solution for German GNSS reference stations is already being operationally delivered to the Deutscher Wetterdienst - The German Meteorological Service for NWM assimilation testing purposes (Bender et al., 2016). Figure 4 shows all the solutions using STDs calculated from the estimated ZTD and horizontal gradient parameters, i.e. without adding post-fit residuals. Adding raw or clean residuals, applied consistently to both compared and reference solutions, provided very similar graphs (not displayed). Colours in Figure 4 indicate the processing software used in individual solutions. Medians of all solutions (dotted lines in each bin) are displayed for each station in order to highlight differences among the stations. These

were observed mainly as biases ranging from -3.6 mm to 0.6 mm. The better agreement between GOP and GFZ solutions could be attributed to a similar strategy of both solutions compared to others. It is particularly visible for LDB0 and POTM stations where median values over all solutions differ by -2.3 mm and -3.6 mm, respectively. The reason for the divergent behaviour at the two stations has not been identified although site metadata were cross-checked carefully. A significant difference can also be noticed for TUW_3 and TUW_7 at the station KIBG where these solutions used individual antenna calibration files while all others solution used type mean calibration (Schmid et al., 2016). On the other hand, plots with standard deviations show agreements within 3-5 mm among all the stations and all solutions. The only exception is the GOP_F solution representing a simulated real-time analysis applying only a Kalman filter (not backward smoothing) and providing results by a factor of 2 worse compared to the others in terms of precision.

#### 7.1.2 Impact of post-fit residuals

All individual GNSS STD solutions were compared independently using none (nonRES), raw (rawRES) and clean (clnRES) residuals. The comparison aimed at assessing the impact of different strategies for reconstructing GNSS STDs. Figure 5 displays biases and standard deviations for all solutions when comparing STDs with and without raw residuals. Similarly, Figure 6 shows results for STDs with and without clean residuals. Both comparisons demonstrate biases at a sub-millimetre level over all stations and solutions. Smaller biases are however observed in the latter case (clnRES) which demonstrates the presence of station-specific systematic errors in raw residuals (over all days of the benchmark) projected into zenith directions. Although the decrease of biases is visible for all solutions, several solutions (GFZ, GOP, WUE) resulted almost with zero values over all the stations. It could be attributed to easier removal of systematic effects in PPP as absolute residuals are accessible directly. This is in contrast to the double-difference solutions by ROB with ZD residuals reconstructed using relative information in original values. Interestingly, the TUW PPP solutions seem to perform similarly to the ROB DD solution in this case.

Comparing standard deviations in both figures demonstrates that the impact of cleaning residuals led to the standard deviations reduced by the factor of 1.2-1.5 over all stations and solutions, namely reaching 2.5-4.5 mm for clean residuals compared to 3.0-6.5 mm resulting from raw residuals. The station-specific behaviour is more obvious for the latter rather than for the former and, generally, the relative performance over all stations is in a good agreement among different solutions applying clean residuals, see Figure 6. In particular, LDB0 and LDB2 stations show high discrepancies for raw residuals, see Figure 5, while their standard deviations were significantly reduced after cleaning the residuals becoming more homogeneous with other stations. In this context it should be noted that the station LDB0 is missing in both ROB solutions since it has been excluded from the network solution during the pre-processing phase due to a lower quality of observations. Besides the GOP_F demonstrating simulated real-time solution, showing about 25 % worse standard deviations compared to other solutions in Figure 6, we can also observe by a 12 % worse performance of the GOP_S solution using forward filtering and backward smoother. Both can be attributed to the stochastic model applied in the GOP software with epoch-wise parameter estimation, and partly also to remaining deficiencies in implementations of all applied models as the only in-house software has been

developed from scratch recently and, in contrast to others, could not have been extensively used in a variety of applications. Finally, there are rather small differences observed due to the applied strategy, namely forward versus backward filtering, GPS versus GPS+GLO and the cut-off 3 versus 7 degrees for elevation angles (statistically compared for STDs above the elevation cut-off angle of 7 degrees).

Table 3 summarizes statistics related to the figures providing medians and standard deviations over all stations. Notably, biases of STDs (over all stations) expressed in the zenith direction are negligible in all solutions, i.e. not affected by adding raw or clean residuals. The impact of adding raw residuals to the estimated model can be characterized by the median RMS of 3.9 mm (first two data columns) which may vary for different stations, e.g. as evident for stations LDB0 and LDB2 in Figure 5 and Figure 6. Adding cleaned residuals shows an overall impact of 2.8 mm (middle data columns) corresponding to the reduction of 29 % compared to raw residuals and up to 50 % for problematic stations such as LDB0 and LDB2. The comparison is understood as the impact of removing systematic errors from the residuals or, in other words, as a degradation of STDs quality when applying uncleaned residuals due to the contamination by systematic errors. From this reason, we would not recommend adding uncleaned (raw) residuals, but cleaned only, when providing STDs from GNSS. However, this comparison does not suggest any preference either for using the estimated model without residuals or a preference of adding clean residuals to reconstruct STDs. Both approaches still comprise of various errors due to approximations, local environmental effects, instrumentation effects or applied models. Additionally, the impact of cleaning the post-fit residuals for the reconstruction of STDs can be characterized by a median standard deviation of 2.6 mm when projected into the zenith direction, roughly 25 mm at the elevation of 6 degrees, which is estimated from differences between STDs using raw and clean residuals over all solutions and stations (last data columns).

### 7.1.3 Evaluation of ZTD processing settings

Individual GNSS solutions provided also variants using the same software and strategy, but with modified settings. This allows us to assess its impact on the estimated parameters, see Table 4. Consequently, we evaluated STDs calculated without residuals expecting the impact (mainly) on estimated ZTDs and horizontal gradients. Biases reached a sub-millimetre level and were almost insignificant with an exception of using GMF versus VMF1 mapping function resulting in a positive bias of +0.94±0.28 mm over all days and stations. Studied effects were sorted by the magnitude of standard deviations. The impact of the elevation angle cut-off (3 ° versus 7 °) resulted in a median of standard deviation below 1 mm, see TUW_3 and TUW_7. In this regard, it is necessary to mention that the difference between those two solutions comes mainly from estimated horizontal tropospheric gradients since no STDs below 7 ° entered the STD validation. The impact of cut-off angle is also dependable on number and quality of observations below 7 ° used in TUW_3 solution. The use of mapping functions based on climatology (GMF) or meteorological (VMF1) data resulted in a slightly larger impact, at the level of 2 mm, which is similar as the impact found for using single (GPS) or dual (GPS+GLO) GNSS constellations. The use of different temporal resolutions of ZTDs and gradients could not be avoided among various contributions due to limited capabilities of handling high number of parameters. An assessment of the temporal resolution is also influenced by applying relative constrains in deterministic approach or setting a

noise level in stochastic process. Anyway, we compared two solutions (ROB_V and TUO_R) using the Bernese software and DD method with the same settings, but different temporal resolutions of ZTDs and gradients. The results show discrepancies at a level of 3 mm which could be partly explained by different sampling, however, we assume also contributions from specific differences in strategies such as data pre-processing. Last but not least, the impact of using Kalman filter for simulating real-time solution compared to the back-smoother (offline) solutions resulted in the discrepancies represented by standard deviation of 4.8 mm.

#### 7.1.4 Evaluation in the slant direction

Figure 7 provides an evaluation of the STDs at their original elevation angles for the station POTS. Four individual panels show bias (top left), normalized bias (NBIAS, top right), standard deviation (bottom left), and normalized standard deviation (NSDEV, bottom right). Normalized bias and normalized standard deviation were computed to see the dependence of relative errors in STDs at different elevations. For its computation, absolute differences of STDs from two solutions were divided by the STD values from the reference solution. For example, when the solution from GFZ (taken here as the reference) was compared against TUO, the standard deviation was computed from all valid absolute differences given as

$$diff\_absolute = STD^i_{GFZ} - STD^i_{TUO} \quad (16)$$

and normalized standard deviation from all valid relative differences given as

$$diff\_relative = (STD^i_{GFZ} - STD^i_{TUO})/STD^i_{GFZ} \quad (17)$$

Since STDs are reconstructed mainly from ZTDs and horizontal gradients, any small differences between the two solutions in the zenith direction should become much larger after mapping down to lower elevations. Therefore, higher values of bias and standard deviation are expected with the decreasing of elevation angle. Indeed, we found that the agreement among individual solutions compared to the GFZ STDs is rather stable above the elevation angle of 30 degrees. Corresponding biases of individual elevation bins are within ±4 mm and standard deviations are slowly increasing up to 10 mm at 30 degrees. With elevation angles decreasing below 30 degrees the biases slightly increase for some solutions.

In terms of standard deviation, the presumption about the dependency of statistics on the elevation angle is clearly visible in the increasing errors with the decreasing elevation angles (Figure 7) while following an exponential decay up to 45 mm at 7 degrees. Normalized standard deviation remains almost constant over all elevation angles indicating a very consistent relative performance of STDs among all the solutions. A similar behaviour is present at all stations although the absolute values can be higher for some stations or solutions, namely GOP_F for LDB0 and WTZZ with standard deviations reaching up to 72 mm.

### 7.2 GNSS versus NWM

STDs from four individual NWM ray-tracing solutions delivered by three different institutions entered the validation (see sections 4.1 - 4.3 for more information). Even the time resolution of NWM is not continuous (only NWM-based results given at 00, 06, 12, and 18 UTC were used), the comparison with GNSS STDs measurements can be used to estimate the quality of the weather prediction. On the other hand, when the meteorological situation is well simulated by NWM, it is relevant for this

study to compare model with GNSS observations. To ensure the consistency of the comparison, only epochs for which STD values were available in all GNSS solutions were considered, i.e. if a single STD value was missing in any GNSS solution, then the STD values at the same epoch were also removed from all other GNSS solutions. This selection of observations and the low time resolution of the NWM models (six hours) led to a restricted set of STDs available for the validation consisting of 9,866 of observations in total.

### 7.2.1 Evaluation of all GNSS solutions without residuals in the zenith direction

Figure 8 presents the comparison of individual NWM STDs and GNSS STDs (without residuals) expressed in the zenith direction. From top to bottom, plots show biases (left) and standard deviations (right) for ALA/BIRA, ERA/GFZ, GFS/GFZ and ALA/WUELS. For most stations, the bias varies between -5 mm and +3 mm for the ALA/BIRA solution, with all GNSS solutions performing similarly. Slightly higher biases and more variability between GNSS solutions are observed at the station POTM. This behaviour is accounted to the GNSS solutions, since POTM and POTS are collocated and the ALA/BIRA provide the same STDs for the validation at both stations. If we exclude both GOP solutions and the GFZ solution the range of biases at station POTM is very similar to range at station POTS. The difference in height of those two stations is 0.5 m. The station POTS is equipped with a choke ring antenna while the station POTM is not, which indicates large multipath effects (see Figure 12) causing higher range of biases for individual solutions at station POTM. Significant biases of approximately -20 mm are present at two Austrian stations, KIBG and SAAL, and being similar for all GNSS solutions. Both stations are situated in the mountainous area south-west of Salzburg city. Since the same biases do not occur at GNSS versus ERA/GFZ nor GNSS versus GFS/GZF comparisons, they are most likely due to a deficiency of the ALADIN-CZ orography representation. Note that ALA/BIRA and ALA/WUELS STDs show an unexpected opposite behaviour for KIBG and SAAL stations (Figure 8), which is related to the difference in the strategy used. This is possibly due to the estimation of the altitude of parameters, their interpolations, and the difference in the step of integration. Except at those two stations, similar biases as for ALA/BIRA can be also found for the GNSS versus ERA/GFZ comparison, ranging from -3 mm to +7 mm (+11 mm at POTM). Although the bias characteristics for GFS/GFZ are practically identical to those obtained for ERA/GFZ, the results for the NCEP GFS model are shifted by approximately +5 mm, resulting into biases ranging from +3 mm to +12 mm (+17 mm at POTM). The origin of this systematic deviation was identified in ZWD values estimated from the GFS model (Douša et al., 2016), and understood as the effect of the lower vertical resolution of NCEP GFS model compared to other NWMs, leading to larger errors in vertical interpolations.

Standard deviations between GNSS STDs and ALA/BIRA, ERA/GFZ and GFS/GFZ solutions are usually around 10 mm when projected into the zenith. Generally, they are higher than the comparison of individual GNSS solutions presented in Section 7.1 and they are also more station dependent. Degradations can be observed at mountainous stations KIBG and SALL for the ERA/GFZ, GFS/GFZ, and ALA/BIRA STDs, reaching standard deviations up to 18 mm in case of the ERA-Interim NWM.

ALA/WUELS solution performed differently compared to all other NWM solutions. It is biased against GNSS solutions, with biases ranging from +9 mm to +25 mm and highest values observed at stations KIBG and SAAL. Standard deviation values are also much higher, by about a factor of 2.5 worse compared to values obtained from the GNSS versus GFS/GFZ comparison. The probable reason for this is that signal tracking was performed for vacuum elevation angles. As we discuss in the following sub-chapter this impact is especially visible at low elevation ray-paths at which the signal has to travel through the troposphere for a longer time, enhancing the negative effect of underestimated delays.

Finally, comparisons between the three versions of GNSS solutions (nonRES, clnRES, rawRES) and the ALA/BIRA, ERA/GFZ, and GFS/GFZ NWM solutions were done to test the influence of post-fit residuals on GNSS STDs. The ALA/WUELS solution was excluded from this comparison because of the lower quality of its STDs. All GNSS solutions without post-fit residuals reached slightly lower standard deviation values than the solutions which included either raw or cleaned post-fit residuals, while differences in biases were negligible (not displayed). An average increase of standard deviation was 4.5 % for clean residuals and 8.3 % for raw residuals. Indeed, because of their low horizontal and time resolution, the used NWP models can barely capture the very fine-scale tropospheric structures which are supposed to be included in the GNSS residuals. As a consequence, this comparison does not allow to conclude clearly on the potential benefits of post-fit residuals in the reconstruction of the GNSS STDs.

### 7.2.2 Evaluation in the slant direction

Statistics from the comparison of ALA/BIRA, ERA/GFZ and GFS/GFZ against all three versions of GNSS GFZ solution expressed at original elevation angles of slant delays are presented for the station POTS in Figure 9. Significantly higher biases can be found at the lowest elevation bin in all three solutions and at all stations (not displayed). At some stations, sudden increases of bias at individual elevation bins were observed. They happened at any elevation angle (different for each NWM STD solution) and were particularly visible in terms of normalized bias. These sudden increases of the bias might origin either in the fact that the model sometimes cannot render the tropospheric structures at their exact locations (unexpected location of high/low values of water vapour partial pressure), or because models running at these resolutions have a tendency to smooth out such tropospheric heterogeneities. Comparing with a model running at convective-permitting scale (e.g. 1 to 4 km) would help to sort out if the origin of such behaviours is to account on the NWP model STD side or on the GNSS STD side.

For all stations, standard deviations present the shape with significantly higher values at elevations below thirty degrees followed by more gentle decrease towards the zenith direction. An exception was found at stations WTZR, WTZS and WTZZ where a rather smooth shape of the curve is disrupted with sudden changes of standard deviation at particular bins over all elevation angles. This implies mainly for GNSS versus ALA/BIRA solution. GNSS versus ERA/GFZ and GNSS versus GFS/GFZ results show such changes less frequently and with lower magnitude by a factor of two or three. Normalized standard deviations vary at all elevation angles for all validated stations without distinct common characteristics. Values range between 0.2 % and 0.9 % with the highest values occurring usually at high lower elevation angles.

Results from the GNSS versus ALA/WUELS solutions (not displayed) show enormous increase of both absolute and normalized bias and standard deviations at low elevation angles below 25 degrees at all stations. It reached biases up to 350 mm and standard deviations up to 300 mm at some stations. Statistical parameters became more stable above 25 degrees, with occasional disturbances similar to those observed in other NWM-based solutions.

#### 7.2.3 Summary of results for GNSS versus NWM

A summary of the GNSS versus NWM validation is presented in Table 5. For each reference station a median of bias and a median of standard deviation in the zenith direction between all GNSS solutions and a particular NWM-based solution are given. If we consider ALA/BIRA and ERA/GFZ only, without the two mountainous stations KIBG and SAAL, absolute biases between NWM and GNSS solutions stay mostly below 3 mm, which represents a very good agreement between these independent sources used for retrieving slant delays. Standard deviations generally range from 8 mm to 12 mm in the zenith projection, with the exception of ALA/WUELS showing lower precision by a factor of 2.5. Statistics stems from the complete benchmark period, and it should be noted that the daily variation of GNSS STDs was much lower than of NWM ray-traced STDs. Significantly higher values of biases and standard deviations were observed at particular days for NWM solutions. A detail evaluation of daily statistics with a respect to the extreme weather conditions is one of the topics that we will study in future.

### 7.3 GNSS versus WVR

Figure 10 compares GNSS and WVR solutions at stations POTM and POTS, in the zenith direction. The number of slant observations which entered the comparison was 32,794 at station POTM and 36,070 at station POTS. Two remarks can be done on the evaluation of biases. Firstly, an overall bias of about 4 mm between the stations POTM and POTS, visible for all GNSS solutions already in Figure 8, indicates a common issue with the GNSS data processing at the station POTM. It was particularly increased for GOP_F, GOP_S and GFZ PPP solutions. Secondly, a bias of about 5.5 mm in the zenith direction can be found between WVR and GNSS solutions even at station POTS. This bias roughly corresponds to 1 kg/m$^2$ of Integrated Water Vapour (IWV), what can be addressed as the achievable accuracy of any technique, however, WVR accuracy is more dependent on a proper instrument calibration.

Values of standard deviation, resulting mostly in 12 mm, are higher than those observed in GNSS versus GNSS comparisons (Section 7.1) and slightly higher than from GNSS versus NWM comparisons (Section 7.2). A cut-off elevation angle of 15 ° was used for the comparison with WVR STDs instead of 7 ° used in other validations. Additionally, it has to be noted that the results can be partly influenced with the settings applied for finding pairs between GNSS and WVR STDs (Section 6). STDs from WVR can thus originate from slightly different azimuth/elevation angles and times than the GNSS ones. All GNSS solutions perform similarly against WVR, with exception of GOP_F due to applying a real-time capable strategy.

The GNSS versus WVR validation at the station POTS using original elevation angles is displayed in Figure 11. Although some differences between GNSS solutions are visible, all of them performed in a very similar manner. The decrease of values

of four statistical parameters strongly follows the increase of elevation angle and, generally, it is steeper than statistics dependency of GNSS versus NWM. It indicates that slant delays from WVR below 40 ° becomes generally unreliable which is particularly clear from normalized biases and standard deviations at lower elevation angles. A sudden increase of the values is observed at elevations of 55–60 degrees most likely originating from WVR observations which has not been understood yet. Generally, standard deviations for all solutions using cleaned residuals (resp. raw residuals) are in average 1.7 % (resp. 3.8 %) higher than for the solutions without residuals. Differences between solutions variants are smaller due to an overall higher uncertainty of WVR observations, however, the results are in a good agreement with those obtained for GNSS versus NWM comparisons presented in Section 7.1.

## 8 Validation of results at collocated stations

Always two erroneous techniques for STD retrievals have been compared in previous sections (GNSS vs. NWM, GNSS vs. WVR) without knowing the true reference. The errors stem from the observation noise on one hand and, from the processing models including the model for adjusted parameters on the other hand. From this perspective, the higher standard deviations for GNSS STD solutions applying clean residuals compared to those using adjusted GNSS parameters only (without residuals) do not necessarily mean the lower quality of the former. GNSS and NWM models with limited temporal and spatial approximations are not able to represent true signal tropospheric delays between a receiver and all visible satellites. The simplifications certainly result in better agreement of STDs without residuals in Eq.1, however, hardly represent the true tropospheric path delays, deviating particularly during the events with high spatio-temporal variations in the troposphere.

For this reasons, we assessed all GNSS solutions at the collocated (dual) stations as for such constellation we are able to provide troposphere-free differences of STDs to evaluate noise of GNSS STD retrievals. We particularly focused on days with a high variability in the troposphere selected from the benchmark period. Dual stations were available in the benchmark campaign at three different locations in Germany. The first two sites collocate twin GNSS reference stations (LDB0+LDB2 and POTM+POTS), the third location collocate three individual reference stations (WTZR+WTZS+WTZZ). Nevertheless, in the case of Wettzell, only results for WTZR+WTZS are presented due to their similarity with the two other combinations at the same place. Characteristics of the stations are summarized in Table 6.

### 8.1 Slant residuals and slant delay differences

STD validations in this paper were done for two months of the benchmark during which heavy rain events occurred for some days, particularly May 31 – June 3, June 9-11 and June 21-26, all causing severe flooding in Central Europe. During normal weather conditions, the tropospheric variation is reasonably smooth, meaning it can be well represented by GNSS STDs reconstructed from ZTDs and horizontal gradients. However, during high temporal or spatial variabilities in the troposphere, post-fit residuals certainly contain tropospheric signals which were not modelled. If they surpass the observation noise and other residual errors from GNSS models, cleaned residuals should be considered in the GNSS STD model as described in Eq.1.

In order to initially address optimal STD modelling under different weather conditions within the benchmark, we tried to identify days with a high variability in the troposphere. Daily standard deviations of cleaned post-fit residuals were computed individually for each day of the benchmark, for every station and GNSS solution for 1-degree elevation angle bins. We studied their daily variations considering the GNSS model applied. If cleaned post-fit residuals consist of the noise of observations only, the variation in time should be negligible. However, the days showing significantly higher values, correlated at all collocated stations, indicate highly variable tropospheric conditions.

Three such days were identified at LDB0, LDB2, POTM and POTS stations (May 31, June 20, June 23) and two days at WTZR and WTZS stations (June 19, June 20). They all very well correspond to the days initiating heavy precipitations in the domain, Douša et al. (2016). Typical differences between raw and clean residuals are displayed in Figure 12 for all elevations during the normal day (June 19, DOY 170) and the day with high variability in the troposphere (DOY 171, June 20) for LDB0, LDB2, POTM and POTS stations using GFZ solution. Obviously, the variability of clean residuals (black dots) and their 2-sigma envelops are higher by a factor of two for the day of year 171 compared to 170. The variability is clearly visible over all elevations, but the increase is slightly higher at low elevations. The plots for these four stations clearly demonstrates the different quality of GNSS observations, particularly related to a multipath effect displayed by 2-sigma envelop (green curves). Low multipath is common to the stations using choke ring antennas, in our case POTS and LDB2, however, LDB2 still suffer from unknown systematic effects at 35-55 ° elevations. Very high multipath effect was observed particularly at LDB0 station over all elevations. Variability of 2-sigma envelopes of clean residuals (red curves) indicates a higher sensitivity of clean residuals to the weather conditions compared to station selection and observation quality, thus suggesting a significant contribution from the troposphere to the cleaned residuals. In the same context, raw residuals show much higher sensitivity to the observation quality compared to different weather conditions, which is particularly true in case of LDB0 and LDB2 stations. Elevation-dependent differences of STDs using clean residuals (black dots) are displayed in Figure 13 for the same days as in Figure 12, selecting GFZ solution and station pairs WTZS–WTZR and LDB0–LDB2. Additionally, 2-sigma envelops are plotted for differences without residuals (red curves), clean residuals (green curves) and raw residuals (blue curves).

Firstly, we can notice that STD differences are more or less similar for both days, i.e. no significantly different between days with normal and high variations in the troposphere which is found common to other days of the benchmark. It suggests that increased residuals in Figure 12 for DOY 171 contain strong contributions from the tropospheric effect that could not have been assimilated into ZTDs and tropospheric horizontal gradients. Alternative explanation suggests a possible contribution of satellites-specific errors common to both receivers, thus easily eliminated in STD differences at the dual stations. However, systematic errors at satellites are well absorbed by initial phase ambiguities in PPP and short-term or random errors, e.g. such as due to satellite clocks, are in this study eliminated by the use of final products, i.e. stable enough to avoid observed day-to-day variability in cleaned residuals. The DOY 171 thus shows the situation when cleaned residuals contain a tropospheric signal that should be added to the STD retrievals. In the case of GFZ, the contribution from residuals is particularly important due to local troposphere variation in time when using model of piece-wise constant function with 15 minutes time resolution for ZTD and 60 minutes for horizontal gradients. It is not so obvious in case of a stochastic process using for epoch-wise

estimates of all tropospheric parameters. However, the uncertainty of estimated parameters is then higher compared to the deterministic model, which is more difficult to separate errors in estimated parameter and errors due to insufficiency of the linearized tropospheric model in time.

Secondly, we can see that envelops of differences using raw residuals are always the largest ones. Raw residuals vary more with the elevation angle, which is particularly visible for differences LDB0–LDB2. Obviously, it is due to the large systematic errors at LDB0 station and additional contribution from LDB2 errors observed at 35-55 ° elevations. The 2-sigma envelops of STD differences with clean residuals smoothly follows the 2-sigma envelop of STDs differences without residuals, keeping the difference within ±15 mm over all elevations. It indicates a stable and reliable usage of clean residuals under any conditions. On the other hand, applying raw residuals at problematic sites may seriously degrade STDs as observed at LDB0 station.

Finally, we can consider that error contribution from both stations to STD differences at dual stations is equal, i.e.

$$\delta^2_{STD\_dif} = 2\,\delta^2_{STD\_res} \tag{18}$$

with $\delta^2_{STD\_dif}$ variance calculated from cleaned STD differences at specific elevations when using the same processing strategy at both dual stations and, with $\delta^2_{STD\_res}$ characterizing the variance over errors in GNSS STD retrievals corresponding to the observation elevation angle and the applied strategy. Although we can notice some differences in $\delta^2_{STD\_dif}$ in collocations, partly due to differences in contributions from both stations, the relative performance of differences from STDs with clean residuals (green curves) and without residuals (red curves) for different days remains similar. Uncertainties of the simplified STDs at low elevations surpass additional uncertainties due to applying clean residuals (green curves vs red curves). According to the magnitude of clean residuals at these elevations (Figure 12), the small uncertainties from calculated differences indicate the presence of tropospheric signals in the residuals at low elevations, roughly below 30 degrees. It seems to be almost independent from the weather conditions and is supposed to represent mainly unmodelled horizontal asymmetry in the troposphere. However, further study on detail impact of residuals on GNSS STDs modelling during severe weather conditions requires longer data set which will be subject of our upcoming study.

Figure 14 displays results for comparisons of individual dual stations in slant directions calculated from all days of the benchmark. The same statistics and plots (not displayed) were prepared also for days identified with ‘severe’ weather conditions, but only minor differences were observed. Strong variations are observed mainly in normalized biases over all elevation angles for the solutions using raw post-fit residuals (rawRES) regardless weather conditions. These are clearly related to local effects such as multipath or modelling instrumented related effects (phase centre offsets and variations) and disappear after using the cleaned residuals (clnRES). The standard deviations and normalized standard deviations at all stations are clearly the lowest for variants without using post-fit residuals (nonRES), slightly higher using cleaned residuals, and significantly higher when using raw residuals, i.e. corresponding to above performed inter-technique validations.

### 8.2 Differences in zenith direction

Table 7 and Table 8 show the statistics expressed in the zenith direction for observations ranging at elevation angles from 7 to 15 and from 15 to 90 degrees, respectively. Median values computed over all GNSS solutions for which residuals were available are presented. Results for the identified days with high daily tropospheric variation are given in the upper part of the table – days are stated in the previous section. In the bottom part results for selected days with low daily variation of post-fit residuals are presented. These days were the same for all collocated stations: May 25, May 30, June 6 (DOY 145, 150, 157). Biases remains stable regardless the severe weather occurrence and if post-fit residuals are used or not. The lowest standard deviations for all dual stations are always related to the solutions without using post-fit residuals. Interestingly, comparing the statistics for STDs evaluated separately for ranges of 7-15 and 15-90 elevation degrees, standard deviations are smaller in high compared to low elevations for variant without using residuals and vice versa for variants using either cleaned or raw residuals. This can be interpreted as the standard GNSS tropospheric model (ZTD and horizontal gradients) represents well observations at elevations above 15 degrees, but suffers by the modelling deficiencies mainly at low elevations. These statistics also supports the above statement that cleaned residuals are valuable particularly for reconstructing low-elevation STDs regardless the weather conditions as they certainly contain non-negligible tropospheric signal from high-order horizontal asymmetry. During the days with high variation of residuals, the standard deviations are usually a little bit higher than during the days with low variation, however, there is no difference between these two regarding the above-mentioned behaviour.

## 9 Conclusions

We presented results of validating tropospheric slant total delays obtained from GNSS data processing with those obtained from NWM ray-tracing, WVR measurements and collocated GNSS stations, in search of the optimal method for estimating GNSS STDs. Ten GNSS reference stations were selected, exploiting data from the 56-day COST ES1206 Benchmark campaign. Eleven GNSS solutions, four NWM-based solutions and one WVR-based dataset entered this validation study. Eight out of eleven GNSS solutions delivered STDs in three variants: 1) without post-fit residuals, 2) with raw post-fit residuals, and 3) with cleaned post-fit residuals. The comparisons were carried out into two scenarios, firstly for STDs at their true elevation angles, and secondly, for STD differences mapped into the zenith direction using a simple mapping function.

Comparisons of STD solutions without residuals, with raw or cleaned residuals were used to study the impact of different strategies for optimally retrieving STDs from GNSS. The impact of cleaning residuals led to the standard deviations reduced by the factor of 1.2-1.5 over all stations and solutions, namely reaching 2.5-4.5 mm in the zenith direction for clean residuals compared to 3.0-6.5 mm resulting from raw residuals, the latter also being highly station dependent. The impact of adding raw or cleaned residuals was practically negligible in terms of biases which remained all the time within ±0.1 mm.

Biases and standard deviations between GNSS and NWM solutions depended on applied ray-tracing method, NWM source and station location. Worse results, by a factor of 2.5 in terms of standard deviation, were observed for the ALA/WUELS solution originating in deficiency of the applied ray-tracing method. Generally, biases in the zenith direction were below ±3

mm for other solutions with the exception of a positive bias of 5 mm observed for GFS NWM model. Standard deviations for all GNSS versus NWM STD comparisons were at the level of 10 mm, excluding the ALA/WUELS solution. Contrary to the GNSS versus GNSS comparisons, normalized standard deviations showed pronounced variability with the elevation angle.

Using the simulation of delays from ALADIN-CZ weather model, we illustrated the impact of the hydrostatic, wet and hydrometeors contributions to zenith and slant delays. These showed strong horizontal variations allowing relevant characterisation of mesoscale meteorological situations. Visualising the slant anisotropic variation of total, hydrostatic, wet and hydrometeor delays in a common sky plot illustrated a weak hydrostatic anisotropy (up to 5.8 mm) which was almost the same as the hydrometeors one (up to 6 mm). The largest anisotropy was induced by water vapour (up to 20 mm), but the total anisotropy was much weaker (12 mm) due to the compensation of mean hydrostatic and hydrometeor anisotropies oriented in the opposite direction.

GNSS STDs from stations POTM and POTS were validated against collocated WVR observations pointed to GNSS satellites. A positive bias of about 5.5 mm and 10 mm was observed for POTS and POTM station, respectively. Standard deviations from comparisons of GNSS versus WVR STDs reached 12 mm in the zenith direction, thus higher compare to NWM solutions. Normalized standard deviations revealed a strong elevation dependency indicating the WVR observations lack the quality at low elevations, particularly below 40 degrees.

Collocated GNSS stations at three different locations were used to evaluate the quality of GNSS STD retrievals applying statistics over troposphere-free STD differences from theoretical point of view. We could observe strong systematic errors in raw residuals at any elevation angles, particularly at stations without the choke ring antenna, such as LDB0 and POTM. We found a strong elevation dependency of bias when using raw residuals which almost vanished when cleaning the residuals from visible systematic errors. It suggests not recommending use of raw residuals, at least without any information about possible systematic errors. Although the simplified STDs reconstructed from the estimated GNSS tropospheric parameters performed the best in all the comparisons, it obviously missed part of tropospheric signals due to non-linear temporal and spatial variations in the troposphere. Identifying low and high variability in the troposphere during all days in the benchmark, we showed that residuals contain significant tropospheric signals in addition to the simplified model, particularly during highly variable troposphere. Additionally, we also identified tropospheric signals at low elevations due to a non-linear horizontal asymmetry in cleaned residuals regardless of the station selection and the quality of its observations. From such finding, we recommend the use of cleaned residuals for an optimal STD retrievals from GNSS, at least for low elevation angles and during a high variability in the troposphere. We also haven't seen any obvious degradation of STD retrievals in other conditions.

The better inter-solution and inter-technique agreements of STDs without residuals compared to those using clean residuals are attributed to the too simple tropospheric model resulting in smooth and robust STDs and, consequently, not containing all interesting signals from the troposphere. The majority of evaluated GNSS solutions used deterministic models with rather long validity of estimated tropospheric parameters for which the residuals are important to overcome modelling deficiencies of low-resolution parameter estimates in time. Our future study will focus on the evaluation of GNSS STDs estimated using a

stochastic process easily applicable in real-time and on a long-term evaluation of azimuthal-dependency of post-fit residuals under severe weather conditions.

**Acknowledgement**

This study has been organised within the E.U. COST Action ES1206 (GNSS4SWEC). The authors thank all the institutions that provided data for the benchmark campaign on which the validation was based on. Namely we want to thank S. Heise (GFZ) for providing the WVR data. The GFS data were provided by the National Centers for Environmental Prediction (www.ncep.noaa.gov). The ERA-interim data were provided by the European Centre for Medium-Range Weather Forecasts (http://www.ecmwf.int/en/forecasts/datasets). M. Kačmařík, J. Douša and P. Václavovic acknowledge the support from the Czech Ministry of Education, Youth and Sports (project no. LD14102). E. Pottiaux (ROB) and H. Brenot (BIRA) acknowledge the support from the Solar-Terrestrial Centre of Excellence (STCE). J. Kapłon and P. Hordyniec (WUELS) acknowledge the support of Polish National Science Centre (project no. UMO-2013/11/D/ST10/03473) for financial support and Wroclaw Center of Networking and Supercomputing (http://www.wcss.wroc.pl) for computational grant using Matlab Software License No: 101979.

**References**

Alber, Ch., Ware, R., Rocken, Ch., Braun, J.: Obtaining single path phase delays from GPS double differences, Geophysical Research Letters, Vol. 27, pp. 2661-2664, doi: 10.1029/2000gl011525, 2000.

Askne, J., and Nordius, H.: Estimation of Tropospheric Delay for Microwaves from Surface Weather Data, Radio Science, 22 (3), 379–386, doi: 10.1029/rs022i003p00379, 1987.

Atmosphere, US Standard. NASA TM-X 74335. National Oceanic and Atmospheric Administration. National Aeronautics and Space Administration and United States Air Force, 1976.

Bauer, H.-S., Wulfmeyer, V., Schwitalla, T., Zus, F. and Grzeschik, M.: Operational assimilation of GPS slant path delay measurements into the MM5 4DVAR system, Tellus A, 63, 2, doi: 10.1111/j.1600-0870.2010.00489.x, 2011.

Bender, M., Dick, G., Wickert, J., Schmidt, T., Shong, S., Gendt, G., Ge, M. and Rothacher, M.: Validation of GPS slant delays using water vapour radiometers and weather models, Meteorologische Zeitschrift, Vol. 6, No. 17, pp. 807-812, doi: 10.1127/0941-2948/2008/0341, 2008.

Bender, M., Dick, G., Wickert, J., Ramatschi, M., Ge, M., Gendt, G., Rothacher, M., Raabe, A. and Tetzlaff, G.: Estimates of the information provided by GPS slant data observed in Germany regarding tomographic applications, J. Geophys. Res., 114, D06303, doi:10.1029/2008JD011008, 2009.

Bender, M., Stosius, R., Zus, F., Dick, G., Wickert, J. and Raabe, A.: GNSS water vapour tomography: Expected improvements by combining GPS, GLONASS and Galileo observations, Advances in Space Research, 47(5), 886–897, doi: 10.1016/j.asr.2010.09.011, 2011.

Bender, M., Stephan, K., Schraff, Ch., Reich, H., Rhodin, A., Potthast, R.: GPS Slant Delay Assimilation for Convective Scale NWP, Fifth International Symposium on Data Assimilation (ISDA), University of Reading, UK, July 18-22, 2016.

Bennitt, E. and Jupp, A.: Operational Assimilation of GPS Zenith Total Delay Observations into the Met Office Numerical Weather Prediction Models, Monthly Weather Review, 140(8), pp. 2706-2719, doi: 10.1175/MWR-D-11-00156.1, 2012.

Bevis, M., Businger, S., Chiswell, S., Herring, T., Anthes, R., Rocken, C. and Ware, R.: GPS Meteorology: Mapping Zenith Wet Delays onto Precipitable Water, Journal of Applied Meteorology, 33, 379–386, doi: 10.1175/1520-0450(1994)033<0379:gmmzwd>2.0.co;2, 1994.

Böhm, J., Werl, B., and Schuh, H.: Troposphere mapping functions for GPS and very long baseline interferometry from European Centre for Medium-Range Weather Forecasts operational analysis data, J. Geophys. Res., 111, B02406, doi:10.1029/2005JB003629, 2006a.

Böhm, J., Niell, A., Tregoning, P., and Schuh, H.: Global MappingFunction (GMF): A new empirical mapping function based on numerical weather model data, Geophys. Res. Lett., 33, L07304, doi:10.1029/2005GL025546, 2006b.

Böhm, J. and Schuh, H.: Vienna mapping functions. In Proc. 16th Working Meeting on European VLBI for Geodesy and Astrometry, pp. 131-143, Leipzig, Germany, Verlag des Bundesamtes für Kartographie und Geodäsie, 2003.

Braun, J., Rocken, Ch. and Ware, R.: Validation of line-of-sight water vapour measurements with GPS, Radio Science, Vol. 36, Num. 3, pp. 459-472, doi: 10.1029/2000rs002353, 2001.

Braun, J., Rocken, Ch. and Liljergen, J.: Comparisons of Line-of-Sight Water Vapor Observations Using the Global Positioning System and a Pointing Microwave Radiometer, Journal of Atmospheric and Oceanic Technology, Vol. 20, pp. 606-612, doi: 10.1175/1520-0426(2003)20<606:colosw>2.0.co;2, 2002.

Brenot, H.: Potential of ground-based GPS measurements for the study of Mediterranean heavy rains. PhD of the French State, http://tel.archives-ouvertes.fr/tel-00012085, 2006.

Brenot, H., Neméghaire, J., Delobbe, L., Clerbaux, N., De Meutter, P., Deckmyn, A., Delcloo, A., Frappez, L. and Van Roozendael, M.: Preliminary signs of the initiation of deep convection by GNSS, Atmos. Chem. Phys., 13, 5425–5449, doi:10.5194/acp-13-5425-2013, 2013.

Chen, G., and Herring, T. A.: Effects of atmospheric azimuthal asymmetry on the analysis of space geodetic data, J. Geophys. Res., 102(B9), 20489–20502, doi:10.1029/97JB01739, 1997.

Dach, R., Lutz, S., Walser, P., and Fridez, P. (Eds): Bernese GNSS Software Version 5.2. User manual, Astronomical Institute, University of Bern, Bern Open Publishing, doi: 10.7892/boris.72297, ISBN: 978-3-906813-05-9, 2015.

Dee, D. P., Uppala, S. M., Simmons, A. J. et al.: The ERA-Interim reanalysis: Configuration and performance of the data assimilation system, Q. J. Roy. Meteor. Soc., 137, 553–597, doi: 10.1002/qj.828, 2011.

Deng, Z., Bender, M., Zus, F., Ge, M., Dick, G., Ramatschi, M., Wickert, J., Löhnert, U. and Schön, S.: Validation of tropospheric slant path delays derived from single and dual frequency GPS receivers, Radio Science, 46, RS6007, doi:10.1029/2011RS004687, 2011.

Douša, J. and Václavovic, P.: Real-time zenith tropospheric delays in support of numerical weather prediction applications. Advances in Space Research, 53(9):1347-1358, doi:10.1016/j.asr.2014.02.021, 2014.

Douša, J., Dick, G., Kačmařík, M., Brožková, R., Zus, F., Brenot, H., Stoycheva, A., Möller, G. and Kaplon, J.: Benchmark campaign and case study episode in Central Europe for development and assessment of advanced GNSS tropospheric models and products, Atmospheric Measurement Techniques, 9, pp. 2989-3008, doi:10.5194/amt-9-2989-2016, 2016.

De Haan, S., Marel, van der H., and Barlag, S.: Comparison of GPS slant delay measurements to a numerical model: case study of a cold front passage, Physis and Chernistry of the Earth, Vol. 27, pp. 317-322, doi: 10.1016/s1474-7065(02)00006-2, 2002.

Flores, A., Rius, A., Vilá-Guearou, J. and Escudero, A.: Spatio-temporal tomography of the lower troposphere using GPS signals, Phys. Chem. Earth (A), Vol. 26, No. 6-8, 405-411, doi: 10.1016/s1464-1895(01)00074-6, 2001.

Gradinarsky, L. P.: Sensing Atmospheric Water Vapor Using Radio Waves, Ph.D. thesis, School of Electrical Engineering, Chalmers University of Technology, Göteborg, Sweden, 2002.

Guerova, G., Bettems, J. M., Brockmann, E. and Matzler, C.: Assimilation of COST 716 Near-Real Time GPS data in the nonhydrostatic limited area model used at MeteoSwiss, Meteorology and Atmospheric Physics, vol. 91, Issue 1-4, pp. 149-164, doi: 10.1007/s00703-005-0110-6, 2006.

Guerova, G., Jones, J., Dousa, J., Dick, G., de Haan, S., Pottiaux, E., Bock, O., Pacione, R., Elgered, G., Vedel, H., and Bender, M.: Review of the state-of-the-art and future prospects of the ground-based GNSS meteorology in Europe, Atmos. Meas. Tech. Discuss., doi:10.5194/amt-2016-125, in review, 2016.

Ha, S.-Y, Kuo, Y.-H., Guo, Y.-R., Rocken, C., and Van Hove, T.: Comparison of GPS slant wet delay measurements with model simulations during the passage of a squall line, Geophysical Research Letters, Vol. 29(23), 28/1-4, doi: 10.1029/2002gl015891, 2002.

Hobiger, T., Ichikawa, R., Koyama, Y. and Kondo, T.: Fast and accurate ray-tracing algorithms for real-time space geodetic applications using numerical weather models. Journal of Geophysical Research: Atmospheres, 113(D20), doi: 10.1029/2008jd010503, 2008.

Kačmařík, M., Douša, J. and Zapletal, J.: Comparison of GPS slant wet delays acquired by different techniques, Acta geodynamica et geomaterialia, Vol. 9, No. 4(168), pp. 427-433, 2012.

Kawabata, T., Shoji, Y., Seko, H. and Saito, K.: A Numerical Study on a Mesoscale Convective System over a Subtropical Island with 4D-Var Assimilation of GPS Slant Total Delays, Journal of the Meteorological Society of Japan, Vol. 91, No. 5, pp. 705-721, doi:10.2151/jmsj.2013-510, 2013.

Lemoine, F. G., Kenyon, S. C., Factor, J. K., Trimmer, R. G., Pavlis, N. K., Chinn, D. S., Cox, C. M., Klosko, S. M., Luthcke, S. B., Torrence, M. H., Wang, Y. M., Williamson, R. G., Pavlis, E. C., Rapp, R. H. and Olson T. R.: The development of the joint NASA GSFC and the National Imagery and Mapping Agency (NIMA) geopotential model EGM96, NASA/TP—1998–206861, doi: 10.1007/978-3-662-03482-8_62, 1998.

Li, X., Zus, F., Lu, C., Dick, G., Ning, T., Ge, M., Wickert, J. and Schuh, H.: Retrieving of atmospheric parameters from multi-GNSS in real time: Validation with water vapor radiometer and numerical weather model, J. Geophys. Res. Atmos., 120, doi:10.1002/2015JD023454, 2015a.

Li, X., Zus, F., Lu, C., Ning, T., Dick, G., Ge, M., Wickert, J. and Schuh, H.: Retrieving high-resolution tropospheric gradients from multiconstellation GNSS observations. Geophysical Research Letters, 42, 4173-4181, doi:10.1002/2015GL063856, 2015b.

MacMillan, D. S.: Atmospheric gradients from very long baseline interferometry observations. Geophys. Res. Lett., 22, 1041–1044, doi:10.1029/95GL00887, 1995.

Mahfouf, J.-F., Ahmed, F., Moll, P. and Teferle, F. N.: Assimilation of zenith total delays in the AROME France convective scale model: a recent assessment, Tellus A, 67, 26106, doi:10.3402/tellusa.v67.26106, 2015.

Möller, G., Wittmann, C., Yan, X., Umnig, E., Joldzic, N. and Weber, R.: 3D ground based GNSS atmospheric tomography, Final Report GNSS-ATom, Austrian Research Promotion Agency (FFG), 9th call, project number 940098, 2016.

Morel, L., Pottiaux, E., Durand, F., Fund, F., Boniface, K., de Oliveira, P.-S. and Van Baelen, J.: Validity and behaviour of tropospheric gradients estimated by GPS in Corsica. Adv. Space Res., http://dx.doi.org/10.1016/j.asr.2014.10.004, 2014.

Nafisi, V., Urquhart, L., Santos, M. and Nievinski, F., Böhm, J., Wijaya, D., Schuh, H., Ardalan, A., Hobiger, T., Ichikawa, R., Zus, F., Wickert, J. and Gegout, P.: Comparison of ray-tracing packages for troposphere delays, IEEE Transactions on Geoscience and Remote Sensing, 50, 469–481, doi:10.1109/TGRS.2011.2160952, 2012.

Rocken C., Sokolovskiy, S., Johnson, J.M., Hunt, D.: Improved Mapping of Tropospheric Delays, Journal of Atmospheric and Oceanic Technology, Vol. 18, pages 1205-1213, doi: 10.1175/1520-0426(2001)018<1205:imotd>2.0.co;2, 2001.

Rueger, J. M.: Refractive index formulae for radio waves, FIG XXII International Congress, USA, April 19-26, 2002.

Saastamoinen, J.: Atmospheric Correction for the Troposphere and Stratosphere in Radio ranging of satellites, Geophys. Monogr. Ser., 15, 247–251, doi: 10.1029/gm015p0247, 1972.

Schmid, R., Dach, R., Collilieux, X., Jäggi, A., Schmitz, M., and Dilssner, F.: Absolute IGS antenna phase center model igs08.atx: status and potential improvements, Journal of Geodesy, Vol. 90, 343-364, doi:10.1007/s00190-015-0876-3, 2016.

Shang-Guan, M., Heise, S., Bender, M., Dick, G., Ramatschi, M. and Wickert, J.: Validation of GPS atmospheric water vapor with WVR data in satellite tracking mode, Ann. Geophys., 33, 55–61, doi:10.5194/angeo-33-55-2015, 2015.

Shoji, J. Nakamura, H., Iwabuchi, T., Aonashi, K., Seko, H., Mishima, K., Itagaki, A., Ichikawa, R. and Ohtani, R.: Tsukuba GPS dense net campaign observation: Improvement in GPS analysis of slant path delay by stacking one-way postfit phase residuals, Journal of the Meteorological Society of Japan, 82, No. 1B, 301–314, doi: 10.2151/jmsj.2004.301, 2004.

Shoji, Y., Kunii, M. and Saito, K.: Assimilation of Nationwide and Global GPS PWV Data for a Heavy Rain Event on 28 July 2008 in Hokuriku and Kinki, Japan, Scientific Online Letters on the Atmosphere, Vol. 5, pp. 45-48, doi:10.2151/sola.2009-012, 2009.

Shoji, Y., Yamauchi, H., Mashiko, W. and Sato, E.: Estimation of Local-scale Precipitable Water Vapor Distribution Around Each GNSS Station Using Slant Path Delay, SOLA, Vol. 10, 29−33, doi:10.2151/sola.2014-007, 2014.

Trojáková, A.: The NWP activities at CHMI, Joint 26th ALADIN Workshop & HIRLAM All Staff Meeting 2016, Lisbon, Portugal, April 4-8, 2016.

Václavovic, P., Douša, J. and Győri, G.: G-Nut software library - state of development and first results, Acta Geodyn. Geomater, Vol. 10, No. 4 (172), pp 431-436, doi:10.13168/AGG.2013.0042, 2013.

Václavovic, P. and Douša, J.: Backward smoothing for precise GNSS applications, Advances in Space Research, 56(8):627-1634, doi:10.1016/j.asr.2015.07.020, 2015.

Vedel, H. and Huang, X.: Impact of Ground Based GPS Data on Numerical Weather Prediction, Journal of the Meteorological Society of Japan, Vol. 82, No. 1B, pp. 459-472, doi: 10.2151/jmsj.2004.459, 2004.

Zumberge, J. F., Heflin, M. B., Jefferson, D. C., Watkins, M. M., and Webb, F. H.: Precise point positioning for the efficient and robust analysis of GPS data from large networks, J. Geophys. Res., 102(B3), 5005–5017, doi:10.1029/96JB03860, 1997.

Zus, F., Bender, M., Deng, Z., Dick, G., Heise, S., Shang-Guan, M. and Wickert, J.: A methodology to compute GPS slant total delays in a numerical weather model, Radio Sci., 47, RS2018, doi:10.1029/2011RS004853, 2012.

Zus, F., Dick, G., Heise, S., Douša, J., and Wickert, J., The rapid and precise computation of GPS slant total delays and mapping factors utilizing a numerical weather model, Radio Science, Vol. 49(3), pp. 207-216, doi: 10.1002/2013rs005280, 2014.

Zus, F., Douša, J., Dick, G. and Wickert, J.: Station specific NWM based tropo parameters for the Benchmark campaign, ES1206-GNSS4WEC COST Workshop, Iceland, March 8-10, 2016.

**Table 1**: Characteristics of 10 GNSS reference stations.

| Name | Latitude [°] | Longitude [°] | Height [m] | Network | Dual station | Receiver | Antenna |
|---|---|---|---|---|---|---|---|
| GOPE | 49.914 | 14.786 | 593 | IGS, EPN | | TPS NET-G3 | TPSCR.G3 TPSH |
| KIBG | 47.449 | 12.309 | 877 | | | TPS GB-1000 | TPSCR3_GGD CONE |
| LDB0 | 52.210 | 14.118 | 160 | | LDB2 | JAVAD TRE_G2T | JAV_GRANT-G3T NONE |
| LDB2 | 52.209 | 14.121 | 160 | | LDB0 | JPS LEGACY | LEIAR25.R4 LEIT |
| POTM | 52.379 | 13.066 | 145 | | POTS | JAVAD TRE_G3TH | JAV_GRANT-G3T NONE |
| POTS | 52.379 | 13.066 | 144 | IGS, EPN | POTM | JAVAD TRE_G3TH DELTA | JAV_RINGANT_G3T NONE |
| SAAL | 47.426 | 12.832 | 796 | | | TPS GB-1000 | TPSCR3_GGD CONE |
| WTZR | 49.144 | 12.879 | 666 | IGS, EPN | WTZS, WTZZ | LEICA GRX1200+GNSS | LEIAR25.R3 LEIT |
| WTZS | 49.145 | 12.895 | 663 | IGS | WTZR, WTZZ | SEPT POLARX2 | LEIAR25.R3 LEIT |
| WTZZ | 49.144 | 12.879 | 666 | IGS | WTZR, WTZS | JAVAD TRE_G3TH DELTA | LEIAR25.R3 LEIT |

**Table 2**: Information about individual GNSS-based STD solutions used in the validation.

| Solution Name | Institution | Strategy | Software | GNSS | Elev. cut-off | Mapping function | Products | ZTD/gradients interval | ZD post-fit residuals |
|---|---|---|---|---|---|---|---|---|---|
| CNAM | ESGT CNAM | DD | GAMIT | GPS | 3 ° | VMF1 | IGS final | 1h / 1h | NO |
| GFZ | GFZ Potsdam | PPP | EPOS 8 | GPS | 7 ° | GMF | GFZ | 15min / 1h | YES |
| GOP_F | GO Pecný | PPP | G-Nut/Tefnut | GPS | 7 ° | GMF | IGS final | 2.5min / 2.5min | YES |
| GOP_S | GO Pecný | PPP | G-Nut/Tefnut | GPS | 7 ° | GMF | IGS final | 2.5min / 2.5min | YES |
| ROB_G | ROB | DD | Bernese 5.2 | GPS+GLO | 3 ° | GMF | CODE final | 15min / 1h | YES |
| ROB_V | ROB | DD | Bernese 5.2 | GPS+GLO | 3 ° | VMF1 | CODE final | 15min / 1h | YES |
| TUO_R | TU Ostrava | DD | Bernese 5.2 | GPS+GLO | 3 ° | VMF1 | CODE final | 1h / 3h | NO |
| TUO_G | TU Ostrava | DD | Bernese 5.2 | GPS | 3 ° | VMF1 | CODE final | 1h / 3h | NO |
| TUW_3 | TU Vienna | PPP | NAPEOS | GPS+GLO | 3 ° | GMF | ESA final | 30min / 1h | YES |
| TUW_7 | TU Vienna | PPP | NAPEOS | GPS+GLO | 7 ° | GMF | ESA final | 30min / 1h | YES |
| WUE | WUELS | PPP | Bernese 5.2 | GPS | 3 ° | VMF1 | CODE final | 2.5min / 1h | YES |

**Table 3**: Statistics from comparisons of individual GNSS STDs (projected in the zenith direction) while using none, raw and clean residuals; median values of biases and standard deviations (SDEV) calculated over all stations with an exception of LDB0 station are given.

| Solution | nonRES – rawRES | | nonRES – clnRES | | rawRES – clnRES | |
|---|---|---|---|---|---|---|
| | Bias [mm] | SDEV [mm] | Bias [mm] | SDEV [mm] | Bias [mm] | SDEV [mm] |
| GFZ | +0.02 ± 0.03 | 3.88 ± 0.51 | -0.01 ± 0.01 | 2.77 ± 0.19 | -0.01 ± 0.03 | 2.73 ± 0.67 |
| GOP_F | -0.00 ± 0.02 | 4.69 ± 0.41 | +0.00 ± 0.01 | 3.43 ± 0.19 | -0.01 ± 0.01 | 3.14 ± 0.50 |
| GOP_S | -0.00 ± 0.01 | 4.39 ± 0.42 | -0.01 ± 0.00 | 3.12 ± 0.16 | -0.01 ± 0.01 | 2.99 ± 0.53 |
| ROB_G | +0.02 ± 0.05 | 3.59 ± 0.66 | +0.02 ± 0.02 | 2.66 ± 0.30 | +0.00 ± 0.04 | 2.37 ± 0.67 |
| ROB_V | +0.01 ± 0.05 | 3.58 ± 0.67 | +0.02 ± 0.02 | 2.66 ± 0.30 | +0.01 ± 0.04 | 2.37 ± 0.67 |
| TUW_3 | +0.03 ± 0.06 | 3.90 ± 0.75 | -0.01 ± 0.04 | 2.85 ± 0.35 | -0.02 ± 0.06 | 2.63 ± 0.78 |
| TUW_7 | +0.04 ± 0.05 | 3.89 ± 0.75 | -0.01 ± 0.04 | 2.80 ± 0.35 | -0.02 ± 0.04 | 2.60 ± 0.78 |
| WUE | +0.02 ± 0.04 | 3.64 ± 0.49 | +0.00 ± 0.01 | 2.54 ± 0.19 | -0.02 ± 0.04 | 2.50 ± 0.66 |

**Table 4**: Impact of selected strategy modifications assessed via comparing individual STDs solution variants. Median values of biases and standard deviations (SDEV) calculated over all stations with an exception of LDB0 station using the estimated model only (without residuals) are given.

| Compared solutions | Remarks on solution differences | | Bias [mm] | SDEV [mm] |
|---|---|---|---|---|
| TUW_3 – TUW_7 | *Elevation angle cut-off:* | 3° versus 7° | +0.46 ± 0.69 | 0.98 ± 0.45 |
| ROB_G – ROB_V | *Mapping function:* | GMF versus VMF1 | +0.94 ± 0.28 | 1.90 ± 0.27 |
| TUO_G – TUO_R | *GNSS observations:* | GPS versus GPS+GLO | +0.18 ± 0.32 | 1.95 ± 0.37 |
| ROB_V – TUO_R | *ZTD/gradient resolution:* | 15min/1h versus 1h/3h | +0.28 ± 0.18 | 3.24 ± 0.30 |
| GOP_F – GOP_S | *Processing strategy:* | Kalman filter versus backward smoothing | -0.60 ± 0.55 | 4.81 ± 0.79 |

**Table 5:** Medians of bias and standard deviation values of differences between all GNSS solutions and a particular NWM-based solution at each reference station, expressed in the zenith direction.

| Station | Bias (mm) | | | | Standard deviation (mm) | | | |
|---|---|---|---|---|---|---|---|---|
| | ALA/BIRA | ERA/GFZ | GFS/GFZ | ALA/WUELS | ALA/BIRA | ERA/GFZ | GFS/GFZ | ALA/WUELS |
| GOPE | 0.3 | 3.3 | 8.6 | 11.5 | 8.3 | 10.3 | 7.1 | 22.4 |
| KIBG | -19.3 | 4.9 | 9.6 | 22.5 | 11.6 | 17.8 | 11.0 | 26.7 |
| LDB0 | -2.0 | 0.7 | 5.5 | 10.6 | 9.9 | 10.3 | 8.5 | 26.2 |
| LDB2 | -1.6 | 0.9 | 6.1 | 15.1 | 9.1 | 10.1 | 8.6 | 25.4 |
| POTM | 3.4 | 6.3 | 12.5 | 18.9 | 8.0 | 10.6 | 9.4 | 26.2 |
| POTS | -1.7 | 1.4 | 7.6 | 12.5 | 7.7 | 10.3 | 9.2 | 25.8 |
| SAAL | -19.4 | 7.8 | 11.7 | 24.3 | 12.7 | 17.9 | 11.8 | 22.9 |
| WTZR | -4.8 | -1.5 | 4.9 | 10.2 | 11.0 | 11.8 | 8.5 | 23.1 |
| WTZS | -3.5 | -0.9 | 4.2 | 10.8 | 11.4 | 12.3 | 8.7 | 23.7 |
| WTZZ | -2.1 | 0.9 | 6.0 | 11.6 | 11.3 | 12.0 | 8.9 | 23.7 |

**Table 6**: Characteristics of individual dual stations.

| Dual station | Location | Horizontal distance (m) | Vertical distance (m) | Identical type of receiver | Identical type of antenna | Pairs of observations |
|---|---|---|---|---|---|---|
| LDB0+LDB2 | Lindenberg | 177 | 0.6 | NO | NO | 143,005 |
| POTM+POTS | Potsdam | 2.5 | -0.5 | NO | NO | 180,636 |
| WTZR+WTZS | Wettzell | 69 | 2.6 | NO | YES | 84,443 |

**Table 7**: Comparison of GNSS STDs from the elevation angles ranging from 7 to 15 degrees at three dual stations; results for days with high daily variability of cleaned post-fit residuals, results for days with low daily variability of post-fit residuals in the bottom part; median values of biases and standard deviations (SDEV) calculated over all GNSS STD solutions are given; statistics are expressed in the zenith direction.

| | nonRES | | clnRES | | rawRES | |
|---|---|---|---|---|---|---|
| | Bias [mm] | SDEV [mm] | Bias [mm] | SDEV [mm] | Bias [mm] | SDEV [mm] |
| Days with high variability of post-fit residuals | | | | | | |
| LDB0+LDB2 | -1.56 | 4.63 | -1.44 | 5.51 | -1.52 | 5.89 |
| POTM+POTS | -5.24 | 1.89 | -5.16 | 3.47 | -5.91 | 4.24 |
| WTZR+WTZS | -0.24 | 2.31 | -0.06 | 3.25 | -0.03 | 3.77 |
| Days with low variability of post-fit residuals | | | | | | |
| LDB0+LDB2 | -0.52 | 3.06 | -0.52 | 4.23 | -0.59 | 5.05 |
| POTM+POTS | -4.97 | 1.87 | -5.03 | 3.00 | -5.79 | 3.87 |
| WTZR+WTZS | -0.01 | 1.87 | -0.05 | 3.22 | -0.09 | 3.82 |

**Table 8**: Comparison of GNSS STDs from the elevation angles ranging from 15 to 90 degrees at three dual stations; results for days with high daily variability of cleaned post-fit residuals, results for days with low daily variability of post-fit residuals in the bottom part; median values of biases and standard deviations (SDEV) calculated over all GNSS STD solutions are given; statistics are expressed in the zenith direction.

5

| | nonRES | | clnRES | | rawRES | |
|---|---|---|---|---|---|---|
| | Bias [mm] | SDEV [mm] | Bias [mm] | SDEV [mm] | Bias [mm] | SDEV [mm] |
| Days with high variability of post-fit residuals | | | | | | |
| LDB0+LDB2 | -0.92 | 4.19 | -0.88 | 6.13 | -0.88 | 8.87 |
| POTM+POTS | -5.28 | 1.68 | -5.30 | 3.39 | -5.30 | 4.64 |
| WTZR+WTZS | -0.53 | 2.29 | -0.56 | 4.12 | -0.49 | 5.21 |
| Days with low variability of post-fit residuals | | | | | | |
| LDB0+LDB2 | -0.07 | 2.59 | -0.07 | 4.93 | 0.04 | 7.83 |
| POTM+POTS | -4.96 | 1.82 | -4.92 | 3.30 | -4.93 | 4.65 |
| WTZR+WTZS | -0.01 | 1.74 | -0.05 | 3.77 | 0.02 | 5.07 |

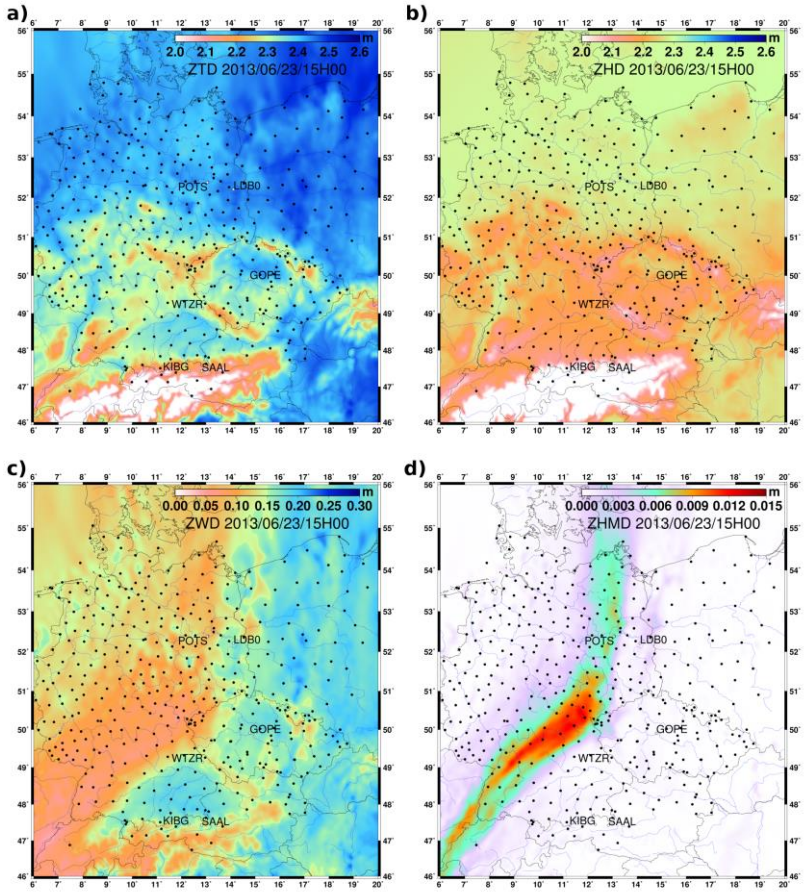


Figure 1: Simulation of ZTD, ZHD, ZWD and ZHMD at 15:00 UTC on 23 June 2013. Each black dot represents a GNSS station included in the benchmark dataset. For stations included in this STD validation study their names are given.

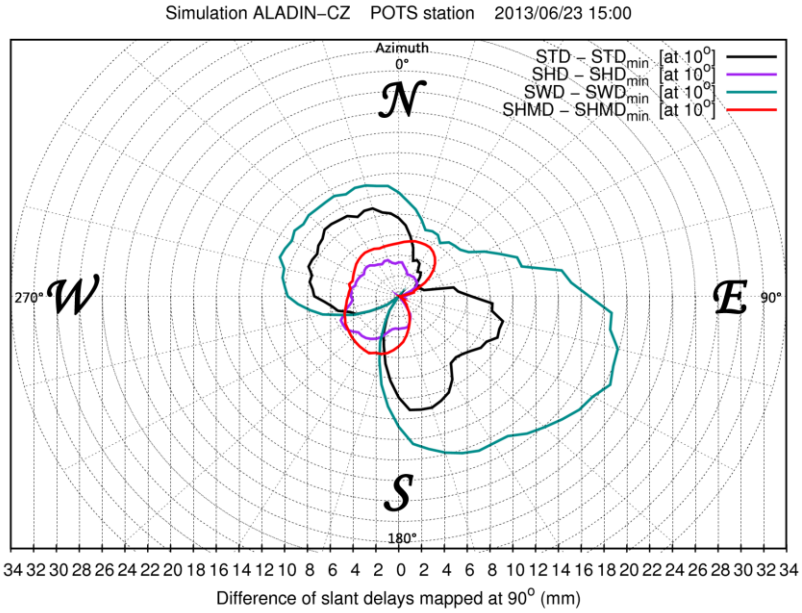


Figure 2: Skyplot of differential slant delays simulated at 10° and mapped at 90°, for a 360° azimuthal range (at 15:00 UTC on 23 June 2013). For total, hydrostatic, wet and hydrometeors delays, a differential slant delay is the difference between a slant delay simulated and the respective minimum value (obtained considering slant delays simulated at 10° elevation along all the azimuthal directions).

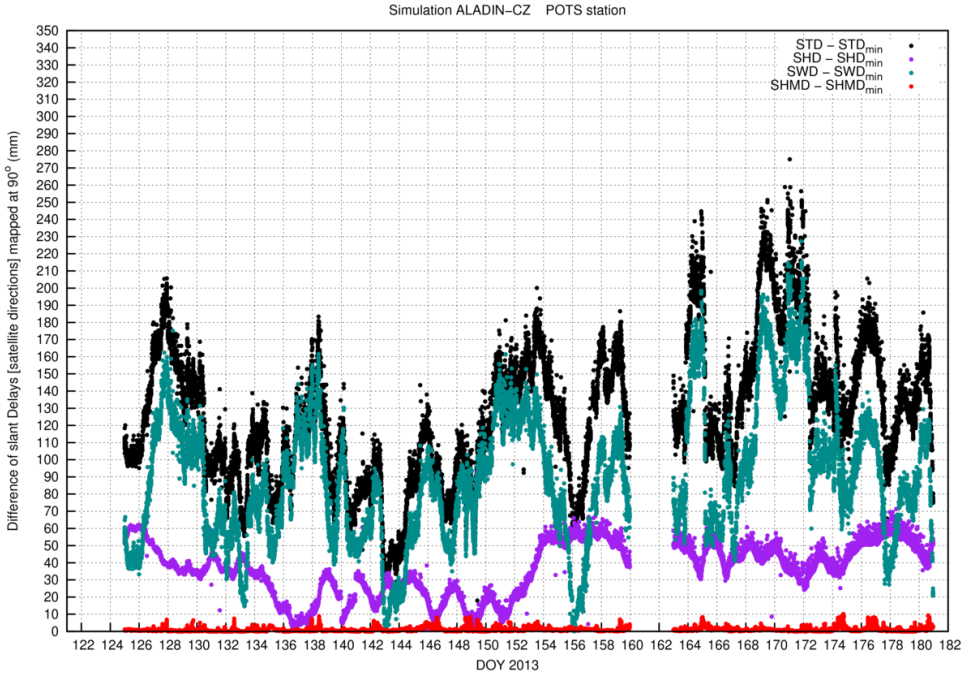


Figure 3: Time-series of slant delays (STD, SHD, SWD, and SHMD) differences (in direction of all GNSS visible satellites, then mapped in the zenith direction) during the whole period of the benchmark campaign for the station POTS.

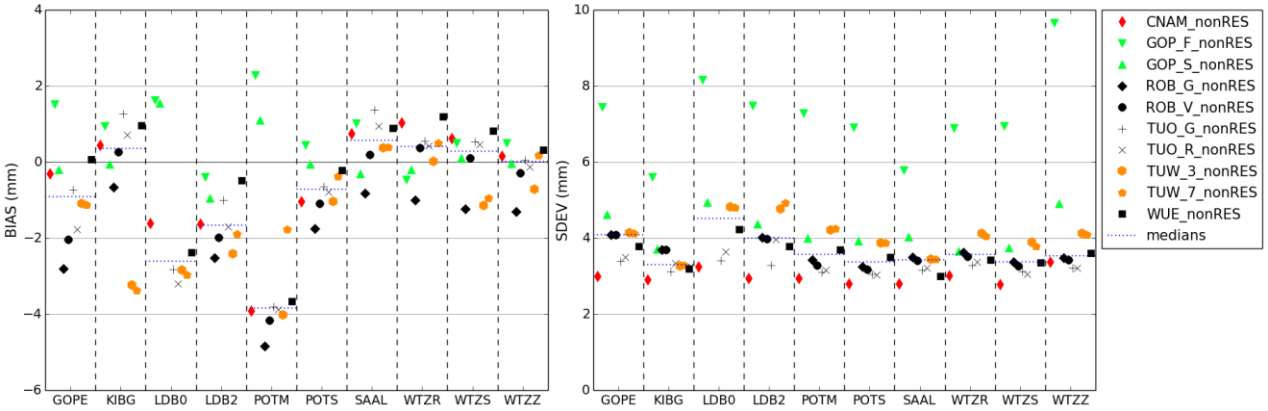


Figure 4: Comparison of individual GNSS STD solutions against GFZ solution, all without using residuals (nonRES) and projected in the zenith direction: bias (left) and standard deviation (right). The median value of all solutions at each station is represented by the dotted blue line in each bin.

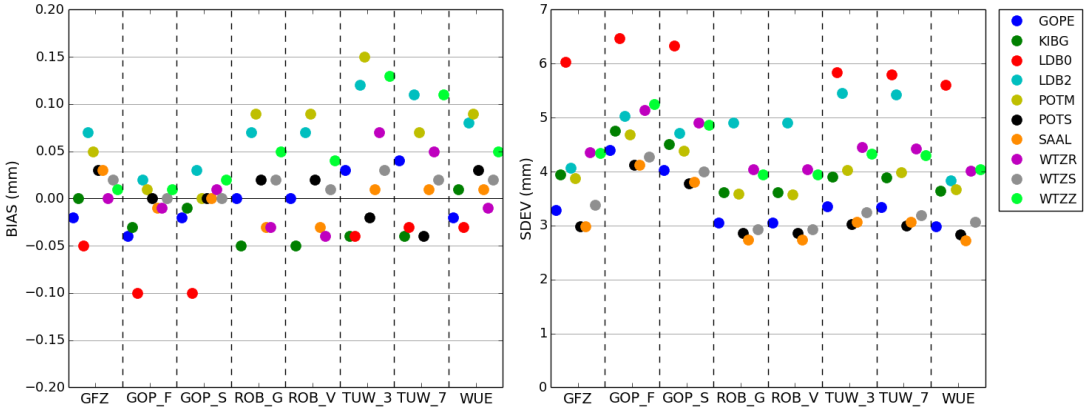


Figure 5: Comparison of individual GNSS STD solutions without residuals (nonRES) and with raw residuals (rawRES); statistics are projected in the zenith direction: bias (left) and standard deviation (right).

5

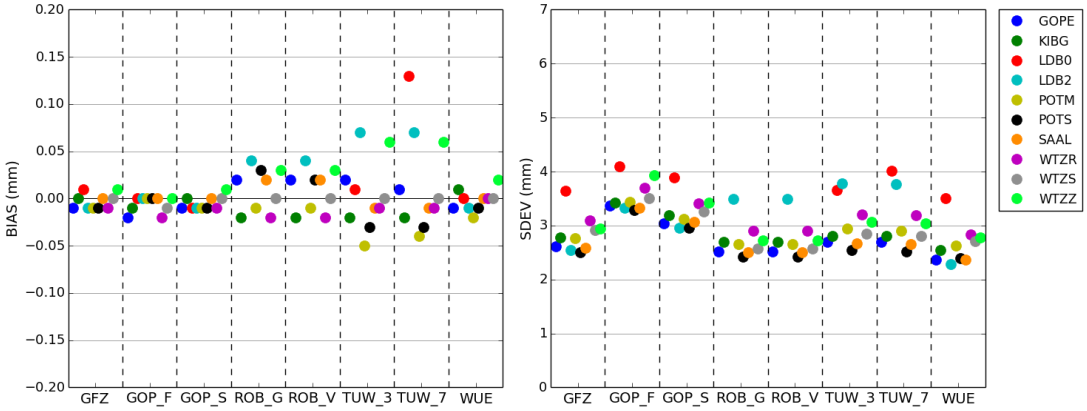


Figure 6: Comparison of individual GNSS STD solutions without residuals (nonRES) and with clean residuals (clnRES); statistics are projected in the zenith direction: bias (left) and standard deviation (right).

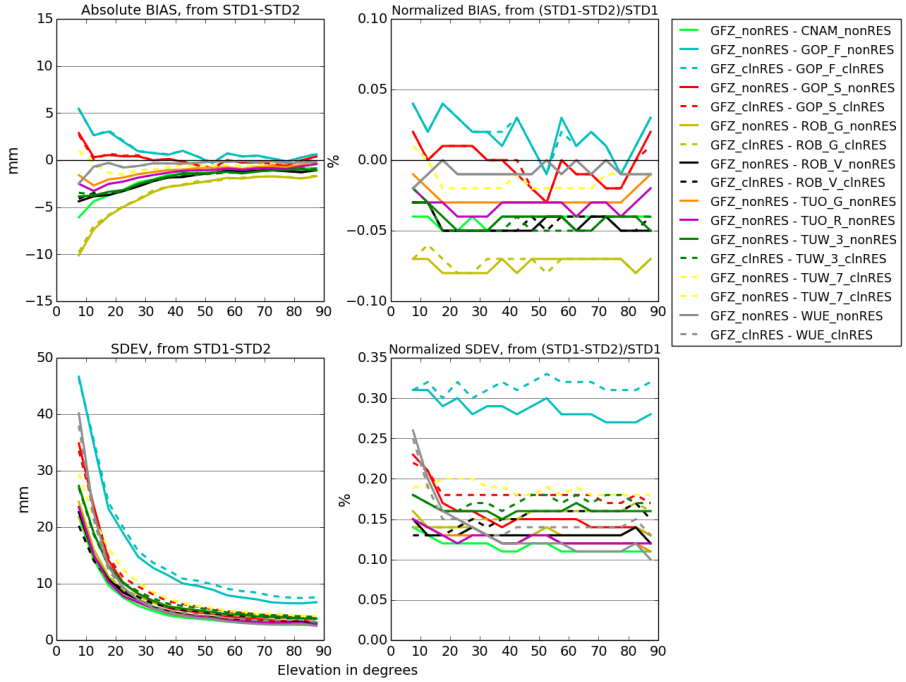


Figure 7: Comparison of individual GNSS STD solutions against GFZ STD solution at station POTS, in slant directions.

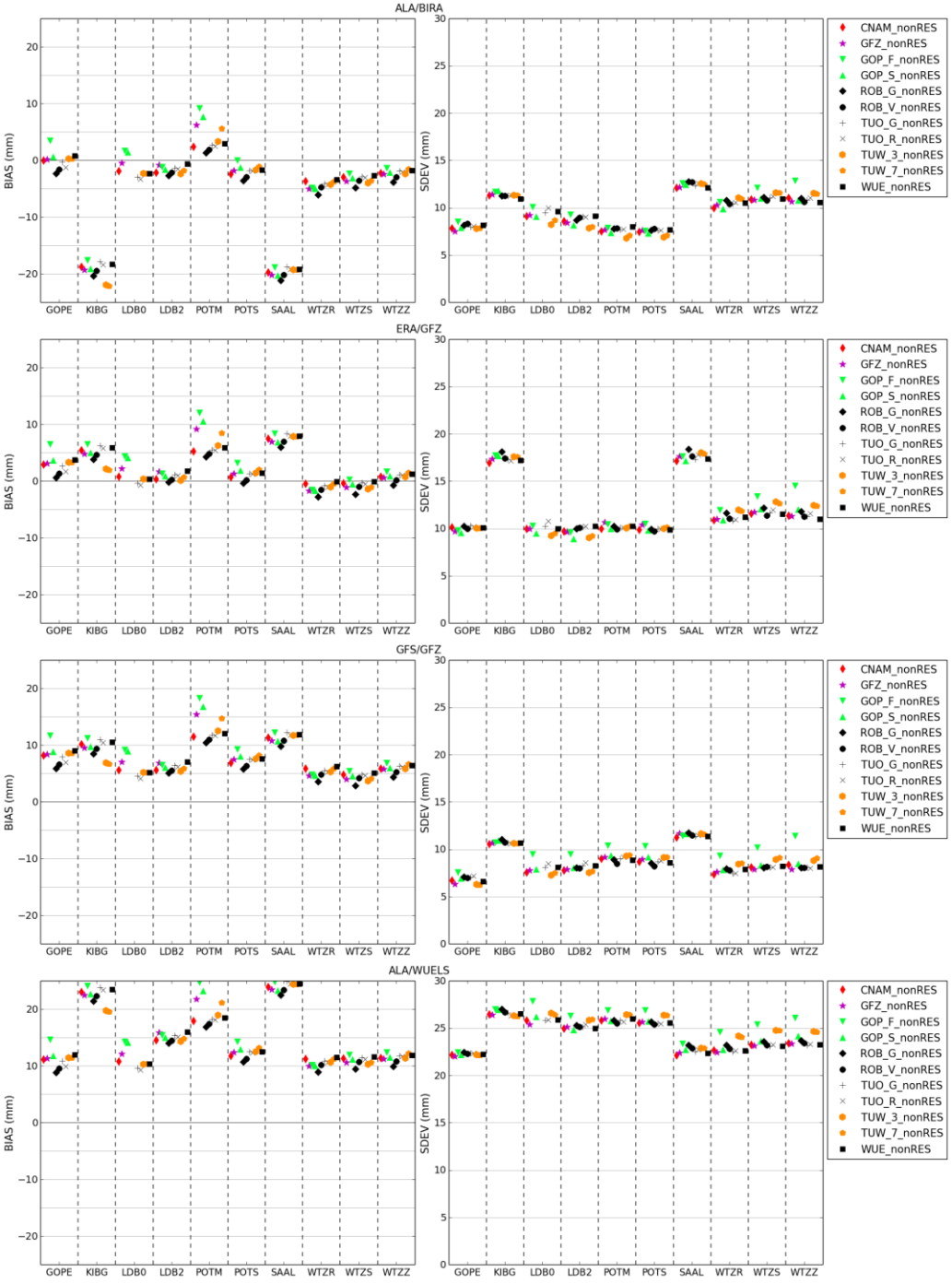


Figure 8: Comparison of individual GNSS STD solutions without residuals (nonRES) against NWM solutions ALA/BIRA, ERA/GFZ, GFS/GFZ, ALA/WUELS (from top to bottom), projected in the zenith direction: bias (left) and standard deviation (right).

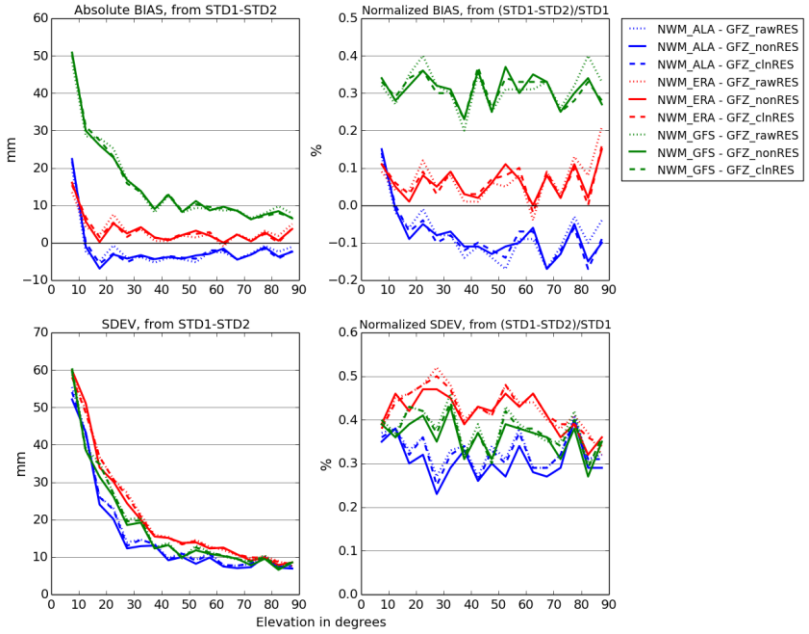


Figure 9: Comparison of NWM-based solutions (ALA/BIRA, ERA/GFZ and GFS/GFZ) against GNSS GFZ solution at station POTS, in the slant direction.

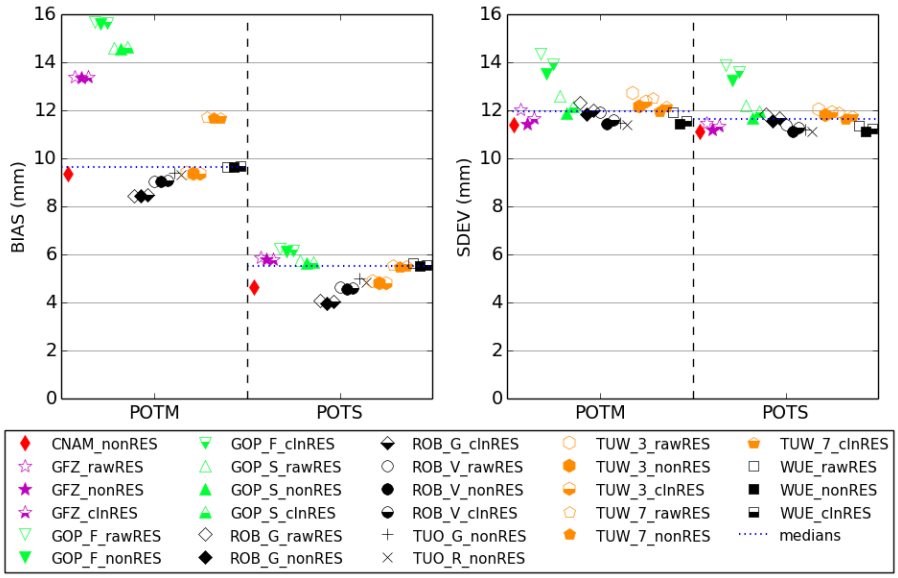


Figure 10: Comparison of individual GNSS STD solutions for stations POTM and POTS versus WVR measurements, expressed in the zenith direction, bias (left) and standard deviation (right). The median value of all solutions at each station is represented by the dotted blue line in each bin.

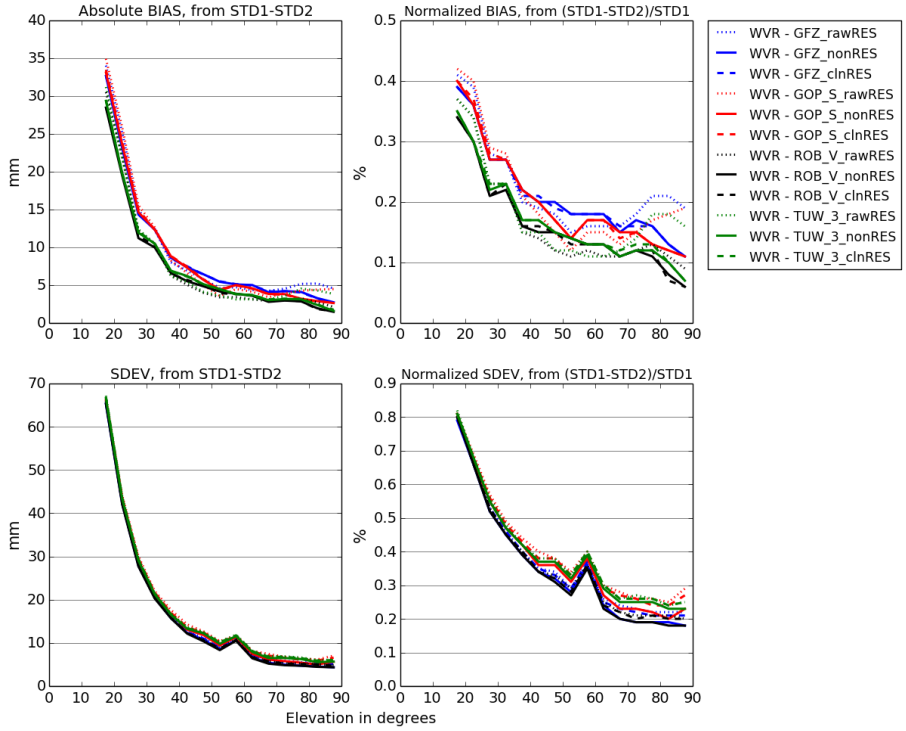


Figure 11: Comparison of WVR against individual GNSS STD solutions at station POTS, in the slant direction.

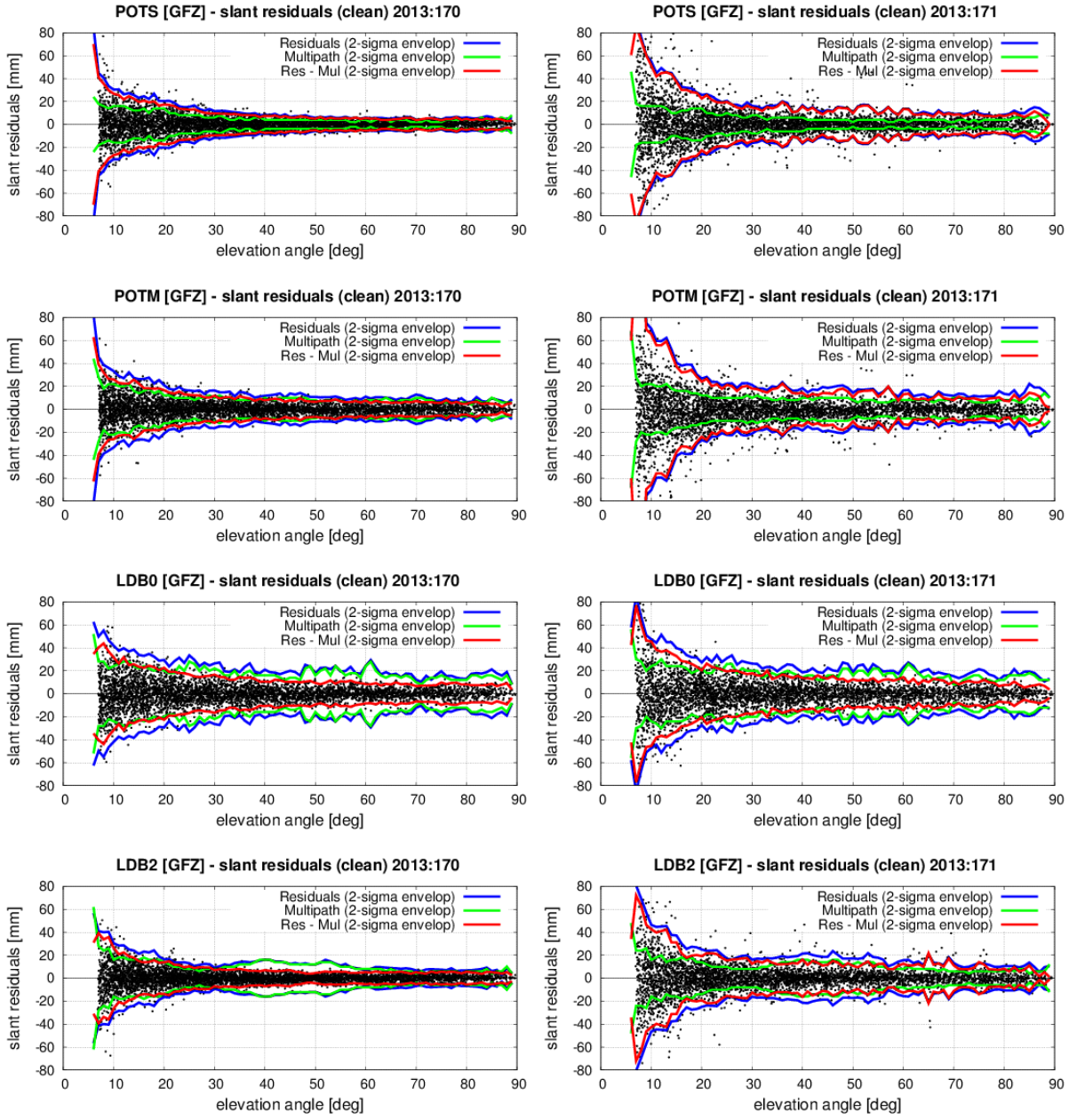


5 Figure 12: Elevation-dependent variability of clean residuals (black dots) and their 2-sigma envelops (red curves) are showed for June 19 (DOY 171) and June 20 (DOY 170) and four stations: POTS, POTM, LDB0 and LDB2. Additionally, plots display 2-sigma envelopes for raw residuals (blue curves) and multipath (green curves).

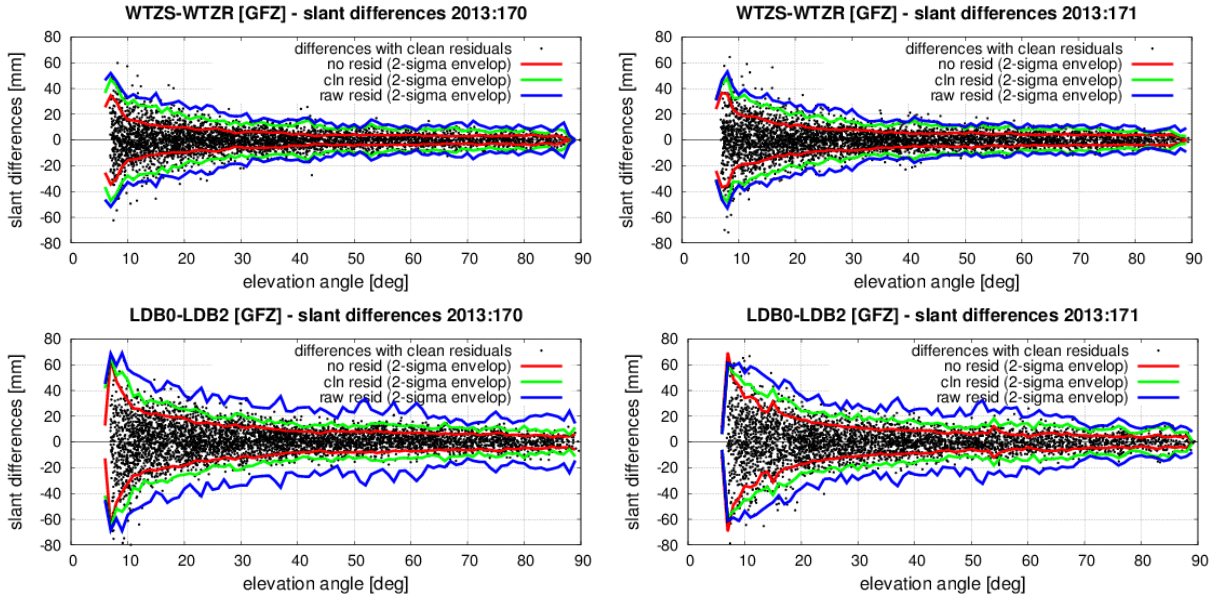


Figure 13: Elevation-dependent variability in STD differences of clean residuals (black dots) and their 2-sigma envelops (green curves) are showed for June 19 (DOY 171) and June 20 (DOY 170) and two dual-stations: WTZS–WTZR and LDB0–LDB2. Plots also display 2-sigma envelopes for differences of raw residuals (blue curves) and without residuals (red curves).

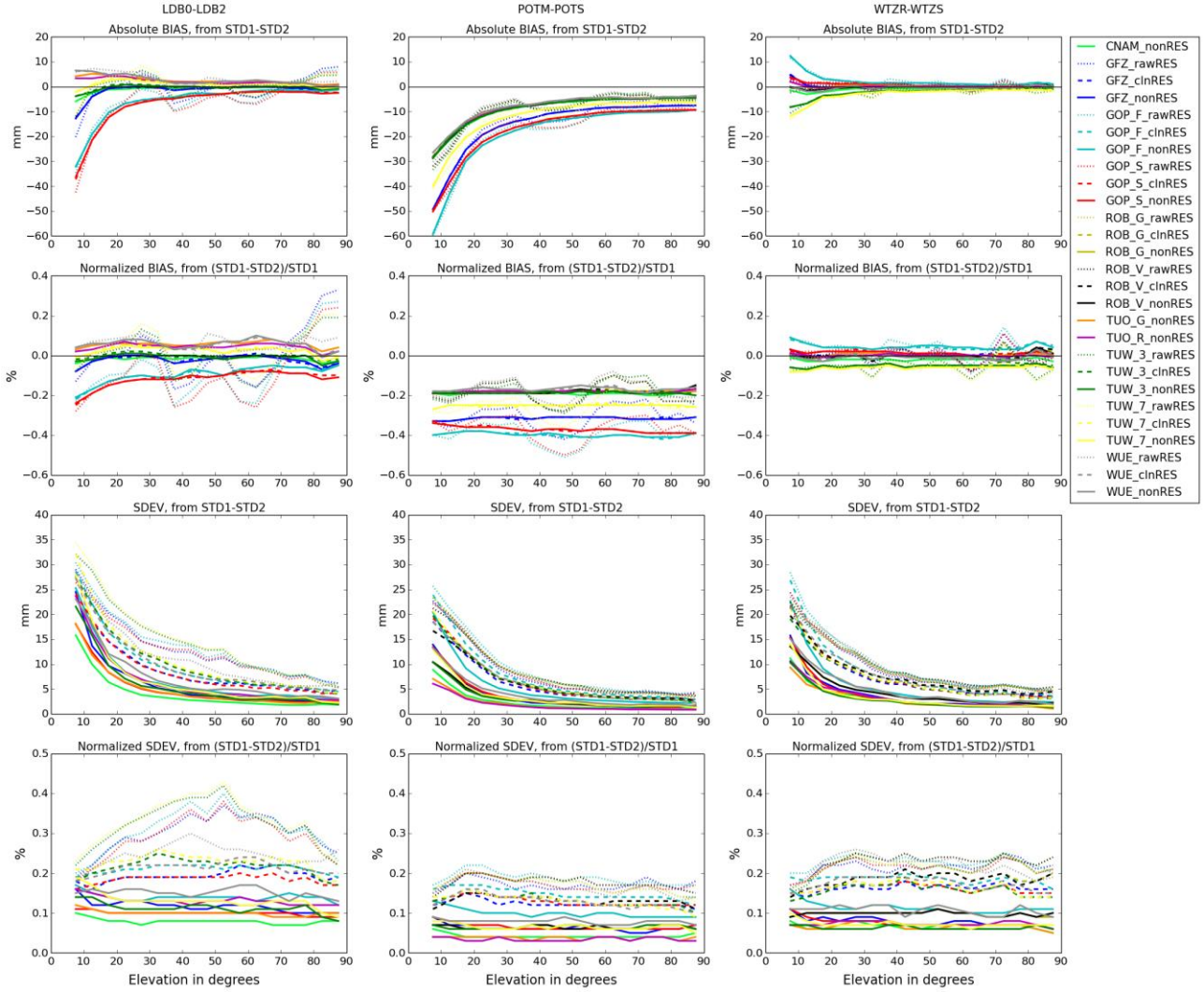


Figure 14: Comparison of GNSS STDs at dual stations computed over whole benchmark period from individual GNSS solutions in the slant direction for dual stations from left to right: LDB0-LDB2, POTM-POTS, WTZR-WTZS. Statistical parameters from top to bottom: bias, normalized bias, standard deviation, normalized standard deviation.